

# On the Acid Sites of Phosphorous Modified Zeosils

Gaurav Kumar<sup>‡</sup>, Limin Ren,<sup>‡,δ</sup> Yutong Pang<sup>‡</sup>, Xinyu Li<sup>‡</sup>, Han Chen,<sup>β</sup> Paul J. Dauenhauer,<sup>‡,δ</sup> Michael Tsapatsis,<sup>‡,δ,ξ,g</sup> Omar A. Abdelrahman,<sup>β,δ,\*</sup>

<sup>‡</sup> Department of Chemical Engineering and Materials Science, University of Minnesota, 421 Washington Avenue SE, Minneapolis, MN 55455.

<sup>β</sup> Department of Chemical Engineering, University of Massachusetts Amherst, 686 N. Pleasant Street, Amherst, MA 01003.

<sup>ξ</sup> Department of Chemical and Biomolecular Engineering & Institute for NanoBioTechnology, Johns Hopkins University, 3400 N. Charles Street, Baltimore, MD 21218.

<sup>g</sup> Johns Hopkins University, Applied Physics Laboratory, 11100 Johns Hopkins Road, Laurel, MD 20723.

<sup>δ</sup> Catalysis Center for Energy Innovation, University of Delaware, 150 Academy Street, Newark, DE 19716.

\*Corresponding Author: abdel@umass.edu

**Abstract.** The acid sites of phosphorus-containing zeosils were probed through a combination of solid acid characterization, density functional theory calculations, and kinetic interrogations, establishing their weakly Brønsted acidic character. Due to the disparity in acid-site strength, P-zeosils catalyzed the probe chemistry of isopropanol dehydration slower than aluminosilicate zeolites by an order of magnitude on an active site basis. Propene selectivity during isopropanol dehydration remained 20-30% higher than that of aluminosilicates, illustrating the distinct nature of the weakly acidic phosphorus active sites that favored unimolecular dehydration routes. Regardless of the confining siliceous environment, the nature of phosphorous active sites was unchanged, indicated by identical apparent uni- and bi-molecular dehydration energy barriers. Kinetic isotope experiments with deuterated isopropanol feeds implicated an E2-type elimination to propene formation on phosphorus-containing materials. Comparison of KIEs between phosphorus-containing zeosils and aluminosilicates pointed to an unchanged isopropanol dehydration mechanism, with changes in apparent energetic barriers attributed to weaker binding on phosphorous-active sites that lead to a relatively destabilized alcohol dimer adsorbate. Both *ex-situ* alkylamine Hofmann elimination and *in-situ* pyridine titration characterization methods exhibited phosphorous acid site counts dependent on probe molecules identity and/or concentration, underpinning the limitations of extending common characterization techniques for Brønsted-acid catalysis to weakly acidic materials.

**1. Introduction.** In the last decade, significant research has been devoted to harness the inexhaustible supply of renewable carbon in lignocellulosic biomass to derive fuels and bulk chemicals.<sup>1,2</sup> Biomass-derived intermediates are replete with multi-functional oxygen moieties (carbonyls, carboxylates, ethers) as well as organic impurities, both of which notoriously lead to coking.<sup>1</sup> Consequently, the use of aluminosilicate zeolites in catalytic chemistries dealing with oxygenate dehydration frequently suffers from poor stability and the need for energy-intensive calcination cycles for regeneration.<sup>2,3</sup> Furthermore, activating these feeds selectively on ‘strongly acidic’ materials is often challenging, and designing new solid-acid catalysts may be required to

efficiently process these alternative feedstock.<sup>1,2,4</sup>

One strategy to address these issues has involved the tuning of solid Brønsted site strength in zeolites to selectively promote desirable pathways, and has relied on the catalytic investigations of trivalent-atom-substituted ([Ga], [Fe], and [B]) zeolites.<sup>5,6</sup> Alternatively, our recent work on exploring selective dehydration catalysts has led to the development of phosphoric-acid supported on all-silica zeolites (with Si/P >10).<sup>7-9</sup> For example, phosphoric acid impregnated on self-pillared pentasil (P-SPP)<sup>10</sup> led to the suppression of undesired alkylation and oligomerization reaction products in the Diels-Alder cycloaddition of ethylene to dimethyl furan, leading to 97% p-xylene yield.<sup>8</sup> Compared to liquid phase phosphoric acid,

reaction rates per phosphorus and selectivities in DMF-to-p-xylene chemistry were increased by using silica supports.<sup>11</sup> Using the same P-SPP catalyst, we demonstrated the selective conversion of tetrahydrofuran and methyltetrahydrofuran to butadiene and pentadienes, respectively.<sup>9</sup> Despite these investigations, phosphorous containing zeosils exhibit catalytic characteristics that have not yet been fully explored, and further advances require a fundamental understanding of their acidic active sites.

A related class of materials, solid phosphoric acid (SPA) catalysts, have been utilized for olefin oligomerization reactions for the better part of the last century.<sup>12–15</sup> However, there are notable differences between them and P-zeosils. For example, while Si-O-P linkages have not been detected on SPA catalysts,<sup>16</sup> their presence has been recently established in P-SPP.<sup>17</sup> Moreover, the support for SPA is either kieselguhr,<sup>18</sup> or pyrogenic/mesoporous silica,<sup>19,20</sup> while P-zeosils have been synthesized using both meso- and microporous supports.<sup>7–9</sup> Lastly, unlike SPA catalysts where only pyrophosphate phases are present, P-zeosils with low phosphorus loadings (Si/P >10) retain the crystallinity and specific surface area of the zeolitic phase.<sup>8</sup> It should be emphasized that P-zeosils are structurally distinct from silicoaluminophosphate (SAPO) zeotypes in that aluminum is not present in the framework,<sup>7–9</sup> and the origin of Brønsted acidity is not a bridged hydroxyl between Si and P,<sup>21,22</sup> but rather terminal P-OH moieties. Despite the industrial prevalence of SPA catalysts, and unlike aluminosilicate analogues like H-ZSM-5, little in the way of fundamental catalytic information is known about P-zeosils. Limited characterization work has pointed to the presence of weak Brønsted acidic centers,<sup>8,23</sup> which is consistent with low reactivity observed in THF ring-opening dehydration reactions.<sup>9</sup>

Benchmarking the performance of P-zeosils using simple probe chemistries, and in doing so, investigating whether traditional acid site counting methods to calculate turnover frequencies can be extended to this class of materials, could contribute to improved understanding of their active sites. To that end, we used kinetic analysis of isopropanol (IPA) dehydration to comment on the identity and counts of active phosphorus species on a variety of all-silica microporous (MFI, BEA), mesoporous (MCM-41, SBA-15, SPP) and non-porous (Stöber)

supports. Our goals are to (a) to compare and contrast the kinetic parameters (Rate-determining step/s (RDS's), site time yields (STY), uni-/bi-molecular dehydration selectivities, and activation barriers) on P-zeosils with aluminosilicate zeolites; (b) assess the implications of weak IPA binding on these sites in dehydration catalysis; and c) investigate changes in the nature of the catalytic P-site with the surrounding environments. More broadly, our results aim to address the challenges in studying catalytic surfaces with low affinity towards substrates, and the findings reported here can be extended to other acid-catalysis applications involving weak adsorbate-surface interactions.

## 2. Results & discussion.

### 2.1 Synthesis and characterization of P-zeosils.

Powder X-ray diffraction patterns (PXRD), scanning electron microscopy images (SEM), and Ar-porosimetry measurements of all synthesized P-zeosils (P-SPP, P-MFI, P-BEA, P-SBA-15, P-Stöber, P-MCM-41) are reported in the supporting information (**Section S.1**), and indicate that the crystallinity, morphology, as well as porosity for the all-silica zeosils is retained after P-loading on all-silica supports, consistent with previous reports on these materials.<sup>8,9</sup> Elemental analyses and textural properties of these synthesized samples are listed in **Table 1**. A detailed <sup>31</sup>P NMR study on the different P-environments on P-SPP has recently revealed a host of mono-, and oligomeric phosphorus environments which evolve with the extent of hydration.<sup>17</sup> We have assumed this to be more broadly applicable across different supports and not independently carried out <sup>31</sup>P solid state NMR characterization of P-zeosils reported here. Since up to now only *ex-situ* NMR has been reported, extrapolating the obtained insights on P-environments to reaction conditions is challenging as accurately quantifying adventitious water (from liquid feeds, gas lines, and as reaction product) is non-trivial.

The reported samples vary from purely microporous (P-MFI and P-BEA), purely mesoporous (P-MCM-41), micro- and mesoporous (P-SBA-15 and P-SPP) to non-porous (P-Stöber); the bulk phosphorous content was held relatively constant across all materials (Si/P ~ 30). Corresponding data for the aluminosilicate zeolite samples has been previously reported in our prior

works: ZSM-5 (Si/Al 40 and 140)),<sup>5,24</sup> Al-BEA (Si/Al 12.5),<sup>5</sup> and Al-SPP (Si/Al 62)<sup>25</sup> and not discussed here for brevity.

**2.2 Brønsted Acidic Protons.** Among techniques to probe solid acids, the Hofmann elimination of primary alkylamines to olefins and ammonia is particularly useful, as it occurs exclusively on Brønsted acidic centers.<sup>26–28</sup> An alkylamine stoichiometrically adsorbed on a BAS (1 mol alkylamine: 1 mol H<sup>+</sup>) reactively desorbs via the Hofmann elimination in the course of a temperature ramp, forming its respective olefin, which is quantified and taken as a measure of the number of accessible BAS. We investigated the utility of this technique to measure the BAS density on P-SPP (Si/P 30) using six different primary alkylamines (n-propylamine (nPA), n-butylamine (nBA), isopropylamine (iPA), cyclopentylamine (cPA), tert-butylamine (tBA), and tert-amylamine (tAA), **Figure 1A**).

The alkylamines varied in proton affinity (918 - 940 kJ mol<sup>-1</sup>) as well as the stability of the carbocation involved in the Hofmann elimination, where a more stable carbocation reacts and desorbs at lower temperatures (in terms of desorption temperatures: nPA~nBA > iPA~cPA > tBA~tAA).<sup>26–28</sup> Over a site-isolated Al-MFI (Si/Al 140), the BAS density remained constant at ~95 μmol H<sup>+</sup> g<sup>-1</sup> within experimental error, independent of alkylamine proton affinity and/or carbocation stability (**Figure 1A**). Conversely, over P-SPP, the measured BAS densities increased seven-fold across the range of alkylamines investigated. Considering pairs of alkylamines with similar carbocation stability (nPA/nBA, iPA/cPA, and tBA/tAA), differences in the measured BAS density revealed a dependence on the proton affinity of the alkylamine. Furthermore, these densities increased with carbocation stability; tertiary alkylamines (tBA, and tAA) yielded significantly higher BAS densities than primary amines (nPA, and nBA).

Measured BAS densities are only reliable if the adsorbed alkylamine reacts first and does not molecularly desorb.<sup>19,20</sup> While this assumption holds true for bridging hydroxyls in aluminosilicates,<sup>29</sup> challenges associated with extending it to weak acids have been previously illustrated on [B]-substituted zeolites.<sup>30,31</sup> Gorte and co-workers have shown that in the course of a TPD, isopropylamine can desorb without reacting on the

weakly Brønsted acidic centers of [B]-substituted MFI, leading to the undercounting of available BAS.<sup>31</sup> On weaker BAS where the barrier to molecular desorption is reduced, the assumption of negligible rates of molecular desorption may not hold true. In addition to the strength of the BAS, alkylamine proton affinity also determines the heat of adsorption and therefore the rate of molecular desorption.<sup>29,31</sup> Therefore, the probability of a pre-adsorbed alkylamine molecularly desorbing as opposed to reactively desorbing through Hofmann elimination will depend on the choice of alkylamine.

To quantitatively probe why these changes in desorption rates are only consequential for P-SPP and not Al-MFI, we compared the rate of reactive desorption via alkylamine Hofmann elimination relative to that of molecular desorption. Considering the Hofmann elimination of tert-butylamine as a representative case, the Arrhenius plots of isobutene formation rates are shown for Al-MFI (same data as reported by Chen et al.<sup>32</sup>) and P-SPP in **Figure 1B**; the apparent elimination activation energy remains within experimental error across the two materials. The observation of similar activation energies is consistent with previous studies suggesting that the kinetics of Hofmann elimination is independent of acid site strength (P-sites and aluminosilicates in this case).<sup>33,34</sup> Conversely, the rate of alkylamine molecular desorption is expected to be considerably larger over the weaker P-acid sites; the calculated tBA adsorption energy on P-MFI (-153 kJ mol<sup>-1</sup>, **Table 2 and Figure S8**) was significantly less exothermic relative to Al-MFI (-229 kJ mol<sup>-1</sup>, **Table 2 and Figure S10**).

The combined effect of the insensitive energetics of Hofmann elimination relative to the varying molecular desorption can be visualized by comparing simulated TPD profiles for each, over Al-MFI and P-SPP. For Hofmann elimination, nearly identical TPD profiles are simulated for both P-SPP and Al-MFI due to identical reaction kinetics (black solid curve in **Figure 1C and D**). On the other hand, the simulated molecular desorption traces (dashed red curves in **Figure 1C and D**) show a sharp contrast; TPD profiles of molecular desorption and Hofmann elimination for tBA over Al-MFI are completely separated by > 100 K (**Figure 1C**). This means that on an aluminosilicate (Al-MFI), the rate of molecular desorption is

significantly lower than the rate of Hofmann elimination such that any adsorbed alkylamine cannot desorb intact before it reacts, leading to all sites being ‘counted’. However, this is not the case for the phosphorus active sites on P-zeosils; significant overlap is expected on P-SPP on account of the accelerated rate of molecular desorption (**Figure 1D**). The proton affinity and/or stability of resulting carbenium therefore influences whether or not the amine desorbs intact or reacts over P-

SPP, with more stable (tertiary carbocation) and more basic (higher proton affinity) amines being able to carry out turnovers on a higher number of active sites. Whether the speciation of the additional sites counted with amines like tBA are identical to those counted with ones like nBA is unknown. Nonetheless, these results, taken together, unambiguously identify P-zeosils as containing weak Brønsted acidic active sites.

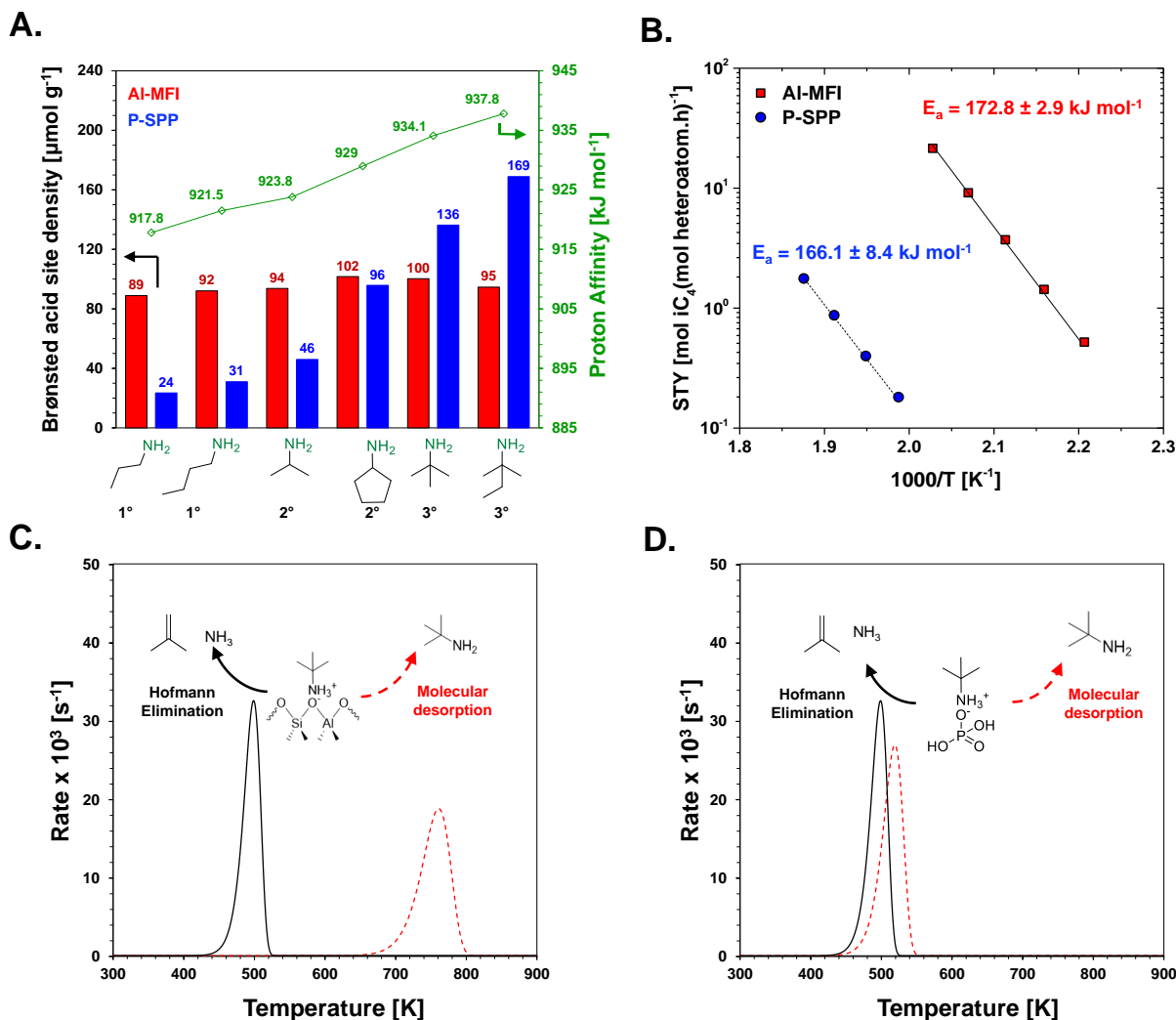


**Figure 1** **A.** (primary axis) The BAS count ( $\mu\text{mol g}_{\text{cat}}^{-1}$ ) of (blue bars) P-SPP (Si/P=30) and (red bars) [H]-ZSM-5 (Si/Al=140) plotted for primary alkylamines; and (secondary axis) Proton affinity ( $\text{kJ mol}^{-1}$ ) for all amines used for the measurement of BAS counts taken from NIST database. (left to right: n-propylamine, n-butylamine, isopropylamine, cyclopentylamine, tert-butylamine, tert-amylamine); **B.** Arrhenius plot for tert-butylamine Hofmann elimination (isobutene formation rates) on P-SPP (●), and Al-MFI (Si/Al 140) (■) (Reaction conditions:  $P_{\text{tBA}} = 10$  torr; WHSV  $2.7 \text{ g g cat}^{-1} \text{ h}^{-1}$  for P-SPP and  $4.4 \text{ g g cat}^{-1} \text{ h}^{-1}$  for Al-MFI, He flowrate = 100 sccm, all conversions below 3.8% for P-SPP and 4.5 % for Al-MFI); **C & D.** TPD simulation of the tert-butylamine (tBA) Hofmann elimination and molecular desorption on Al-MFI and P-SPP, respectively. The solid black line is the calculated TPD based on measured kinetics of tBA Hofmann elimination reported in **B.**, while the dashed red line is the expected desorption TPD if tBA was to desorb intact. The simulations are based on the Polanyi-Wigner equation (See methods for details).



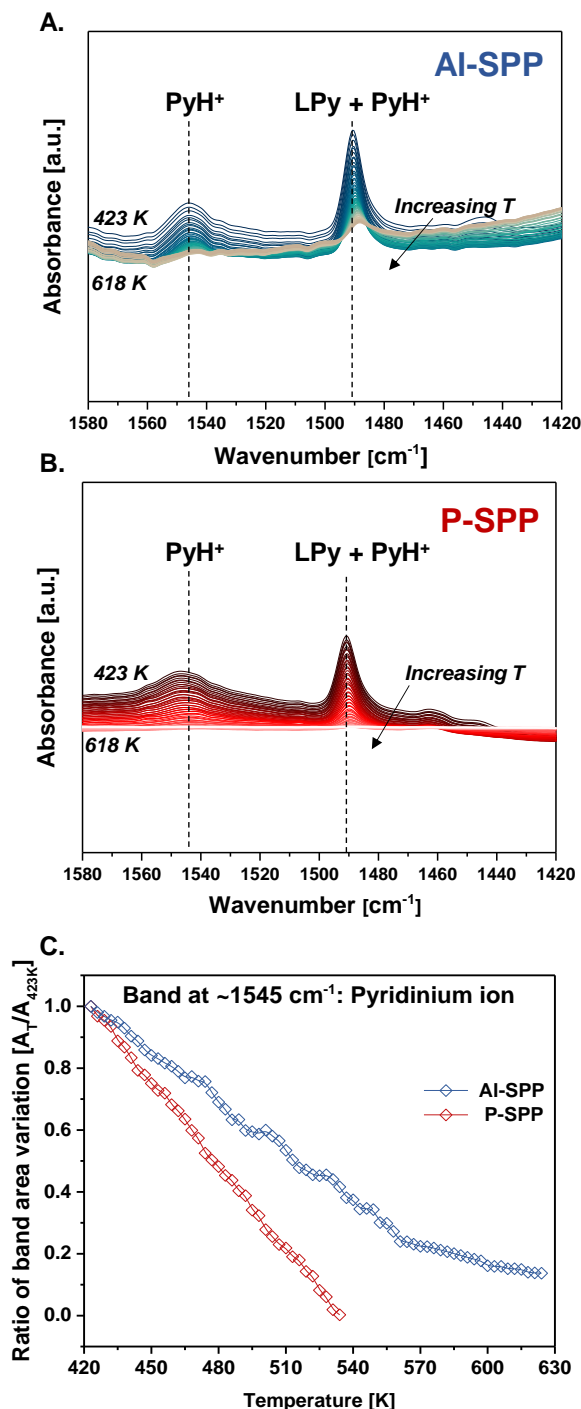


**Figure 2.** IR spectra obtained during the temperature-programmed desorption of pyridine from **A.** Al-SPP (Si/Al 62) and **B.** P-SPP (Si/P 30); **C.** Pyridinium peak band area (~1545 cm<sup>-1</sup>) normalized to initial value (at 423 K) compared for Al-SPP and P-SPP as a function of temperature.

**2.3 Brønsted acidic protons probed by interaction with Pyridine.** In addition to primary alkylamine Hofmann elimination, we investigated the interaction of pyridine with the weak P-sites of P-SPP using a combination of temperature-programmed desorption (TPD) and IR spectroscopy. Analogous experiments with Al-SPP were also carried out for comparison (**Figure 2A**). The IR band at 1545 cm<sup>-1</sup> is characteristic of pyridine adsorbed on Brønsted acid sites, forming a pyridinium ion via complete proton transfer. Despite their weaker acidity, P-zeosils were able to protonate pyridine, evidenced by the characteristic pyridinium ion band (**Figure 2B**). As the temperature was increased, the pyridinium band integrated area decreased on both Al- and P-SPP. While pyridine desorption from the surface of P-SPP was complete at a relatively mild temperature of ~523 K, a non-negligible fraction remained adsorbed on Al-SPP (**Figure 2C**), consistent with the conclusion of weaker acidity of phosphorous based BAS relative to aluminosilicates based on Hofmann elimination (**Sec. 2.2**).

**2.4 Isopropanol dehydration on P-zeosils.** Alcohol dehydration has been extensively used as a probe reaction to characterize acidity in zeotype materials,<sup>6,35–38</sup> and recent computational as well as experimental studies have led to detailed understanding of underlying reaction mechanisms and pathways of light (C1–C4) alcohol dehydration on solid acid catalysts.<sup>37,39–47</sup> The ubiquitous themes tying these studies together are:

- (i) the evidence for the coupling of unimolecular and bimolecular dehydration pathways, where adsorbed dimers that produce di-alkyl ethers (bimolecular dehydration product) can also contribute to olefin formation (unimolecular dehydration product),<sup>43,44</sup>
- (ii) inhibition of olefin formation rates at high alcohol partial pressures (> 50 torr) due to the higher stability of adsorbed alcohol dimers relative to monomers,<sup>37,39</sup> and
- (iii) an increased preference to unimolecular dehydration with increasing temperatures.<sup>37,39,43,44</sup>

The favorability of E1/E2 elimination pathways during alcohol dehydration on zeolites depends on the stability of carbenium formed during the prominence of E2 type pathways as the RDS for isopropanol (a secondary alcohol) dehydration in

aluminosilicates MFI,<sup>41,48</sup> and FAU,<sup>41</sup> while primary alcohol dehydration primarily occurs through E1-type elimination pathways.<sup>37,39,40,43–47</sup> To better understand the active centers of P-zeosils, we sought to compare the kinetics of isopropanol (IPA) dehydration over the two families of catalysts (aluminosilicates and P-zeosils).

#### 2.4.1. Rate and selectivity towards propene.

Across the various phosphorus-containing samples, propene was found to be the dominant product under reaction conditions (**Table 1**). Active P-sites exhibited a preference to unimolecular dehydration relative to their aluminosilicate analogs (e.g., P-MFI versus Al-MFI in **Table 1**, respectively), where selectivity to propene was  $\sim 30\%$  higher. The differences in selectivity are in agreement with aqueous-phase secondary alcohol dehydration studied by Lercher and co-workers, in which bimolecular dehydration of cyclohexanol, 3-heptanol, and 2-methyl-3-hexanol was minimal using aqueous  $\text{H}_3\text{PO}_4$  but prevalent over Al-BEA.<sup>49,50</sup>

Within the family of phosphorous containing catalysts, SPP and MFI structures exhibited the largest activity per mol of bulk phosphorus content, suggesting that the zeolite structure may influence phosphorus active site speciation. However, despite the varying activities per bulk phosphorus content, the apparent energetics of dehydration across the various P-zeosils remain relatively unchanged within experimental error. Over P-SPP, propene formation faces an apparent activation energy of  $\sim 112 \text{ kJ mol}^{-1}$ , with only minor differences among different silica supports (**Figure 3A**). Similarly, apparent bimolecular dehydration barriers to DIPE formation remained nearly constant at  $\sim 75 \text{ kJ mol}^{-1}$  (**Figure 3B**). The relative trend of the apparent barriers was also consistent with prior reports,<sup>44,45,47</sup> where the apparent barrier to unimolecular dehydration was found to be larger than that of bimolecular dehydration (**Figure 3C**). Given that the activation energetics of alcohol dehydration are sensitive to the nature of the active site,<sup>39</sup> the identical activation energies signal that the nature

of active P-sites is unchanged across the different phosphorus containing materials. The observed differences in the bulk-phosphorus normalized rates are likely due to differences in the relative amounts of available catalytic phosphorus sites.

Comparing the overall rate of dehydration across the two classes of materials, aluminosilicates were significantly more active on a heteroatom basis. At a fixed temperature of 403 K, the overall site time yield (STY) of isopropanol (IPA) dehydration over aluminosilicates and P-zeosils is  $\sim 20 \text{ mol C}_3\text{H}_7\text{OH (mol Al. h)}^{-1}$  and  $\sim 0.1 \text{ mol C}_3\text{H}_7\text{OH (mol P. h)}^{-1}$ , respectively. Interestingly, despite the lower rate of dehydration, the phosphorous containing catalysts exhibited a smaller apparent activation energy; the apparent barrier to propene and di-isopropyl ether (DIPE) formation over P-zeosils are both lower by  $\sim 35 \text{ kJ mol}^{-1}$  relative to their aluminosilicate counterparts (**Table 1**).

To understand this seemingly contradictory result, it is necessary to consider the ‘apparent’ nature of the reported activation energies; macroscopically measurable apparent activation energies frequently include thermodynamic contributions like reactant adsorption energies ( $E_{a,\text{app}} = f(\Delta H_{\text{ads}})$ ).<sup>32,51,52</sup> Computationally calculated adsorption energies of relevant surface species (IPA and DIPE) are significantly different on aluminosilicates and phosphorous containing materials ( $\Delta\Delta E_{\text{ads,IPA}} = 13 \text{ kJ mol}^{-1}$  and  $\Delta\Delta E_{\text{ads,DIPE}} = 59 \text{ kJ mol}^{-1}$ , **Table 2**), making the direct comparison of measured activation energies across the two classes of materials non-trivial. Under identical reaction conditions, barriers over aluminosilicates are likely measured from an adsorbed state due to high surface monomer and dimer coverages (in black, **Figure 4A**), and from the gas-phase as reference on P-zeosils due to low coverages (in red, **Figure 4A**). As such, the apparent activation energies values for P-zeosils likely have larger contributions of IPA monomer and dimer adsorption enthalpies, which reduces the apparent activation energy relative to the intrinsic surface activation energy.

**Table 1. Structural and IPA dehydration related catalytic properties of all phosphorus-containing and aluminosilicate zeolites**

Catalyst	Si/X <sup>a</sup>	E <sub>a,unimolecular</sub> <sup>b</sup> [kJ mol <sup>-1</sup> ]	E <sub>a,bimolecular</sub> <sup>c</sup> [kJ mol <sup>-1</sup> ]	Temperature [K]	Sel <sub>unimolecular</sub> [%C] <sup>d</sup>	STY <sub>Dehyd.</sub> [mol IPA (mol P h) <sup>-1</sup> ] <sup>d</sup>
<i>Phosphorous containing</i>						
P-SPP	30.2	114.6 ± 2.5	77.4 ± 1.7	403	83.1	0.21
				423	89.1	0.91
				443	92.9	3.92
P-MFI	36.3	113.4 ± 3.8	75.3 ± 8.8	403	87.5	0.29
				423	92.8	1.31
				443	95.2	5.52
P-BEA	43.1	102.9 ± 3.3	70.7 ± 2.5	403	71.5	0.03
				423	77.3	0.11
				443	85.8	0.42
P-MCM-41	35.5	118.4 ± 4.2	81.2 ± 6.3	403	80.1	0.03
				423	86.3	0.13
				443	91.2	0.58
P-SBA-15	34.5	112.5 ± 8.8	74.5 ± 6.3	403	64.2	0.05
				413	66.7	0.09
				423	65.8	0.19
P-Stöber	32.0	102.9 ± 3.3	77.4 ± 6.3	403	92.6	0.08
				423	94.3	0.31
				443	96.1	1.16
<i>Aluminosilicates</i>						
Al-MFI	40	149.4 ± 1.3	125.5 ± 11.3	393	48.4	5.5
				403	53.3	15.8
				413	63.9	42.2
Al-BEA	12.5	139.3 ± 11.7	101.7 ± 14.6	373	17.2	1.4
				393	22.4	9.3
				403	28.1	22.7
Al-SPP	62	154.0 ± 5.4	129.7 ± 7.1	373	55.5	0.6
				393	64.1	7.6
				403	63.6	17.6

<sup>a</sup> ICP-OES (Galbraith Laboratories); <sup>b</sup> Calculated from the Arrhenius plots of propene formation rates at a fixed  $P_{IPA} = 30$  torr in the temperature range 403-453 K and 373-413 K for aluminosilicates and for P-containing materials, respectively; <sup>c</sup> Calculated from the Arrhenius plots of di-isopropyl ether formation rates in the temperature range 373-453 K; <sup>d</sup> Selectivities and rates measured during IPA dehydration under following reaction conditions:  $P_{IPA} = 30$  torr, WHSV in the range 2.0 – 60.4 g IPA<sup>-1</sup> g.cat<sup>-1</sup> h, all conversions < 8.5%. All values at 403 K have been bolded for easy comparison between P-zeolites and aluminosilicate zeolites at a common temperature.

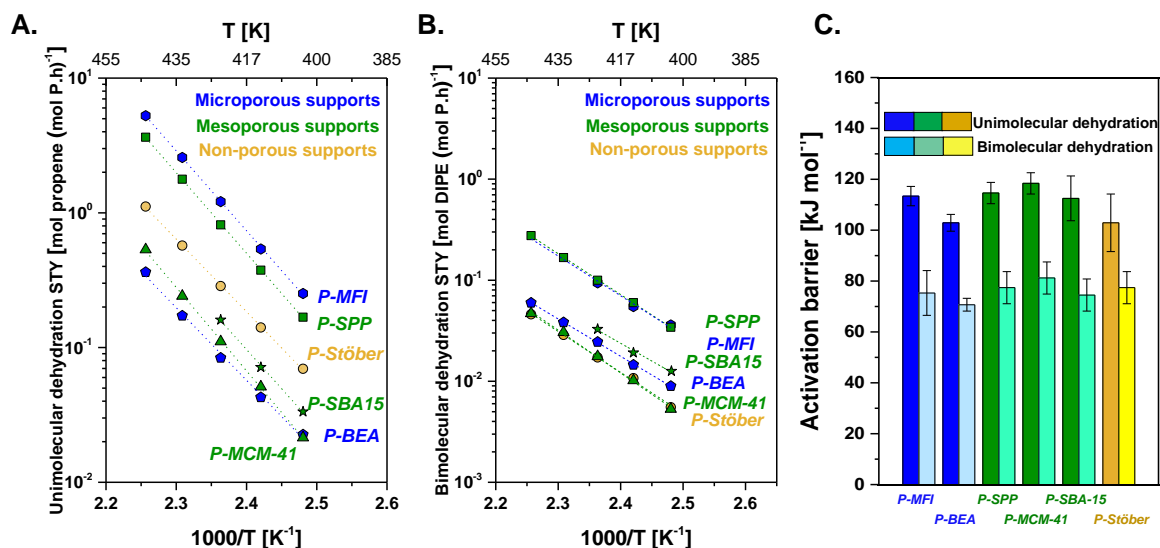


**Figure 3.** A. Arrhenius plot for the unimolecular IPA dehydration rates (propene formation STYs) on all investigated P-zeosils; B. Arrhenius plot for the bimolecular IPA dehydration rates (DIPE formation STYs) on all investigated P-zeosils; C. Activation barriers of unimolecular and bimolecular dehydration compared for all investigated P-zeosils (Reaction conditions: T= 402 – 454 K; WHSV 2.0 – 5.9 g IPA g. cat<sup>-1</sup> h<sup>-1</sup>, diluent (He) flowrate 25 sccm, all conversions < 5%).

**Table 2.** DFT-calculated adsorption energies for surface species on active site in P-MFI and Al-MFI

Molecule	$\Delta E_{\text{ads}}$ [kJ mol <sup>-1</sup> ]		$\Delta\Delta E_{\text{ads}}$ [kJ mol <sup>-1</sup> ]
	P-active site	BAS in Al-MFI	
Tert-butylamine (tBA)	-153	-229	-76
Isopropanol (IPA)	-108	-121	-13
Di-isopropyl ether (DIPE)	-123	-182	-59

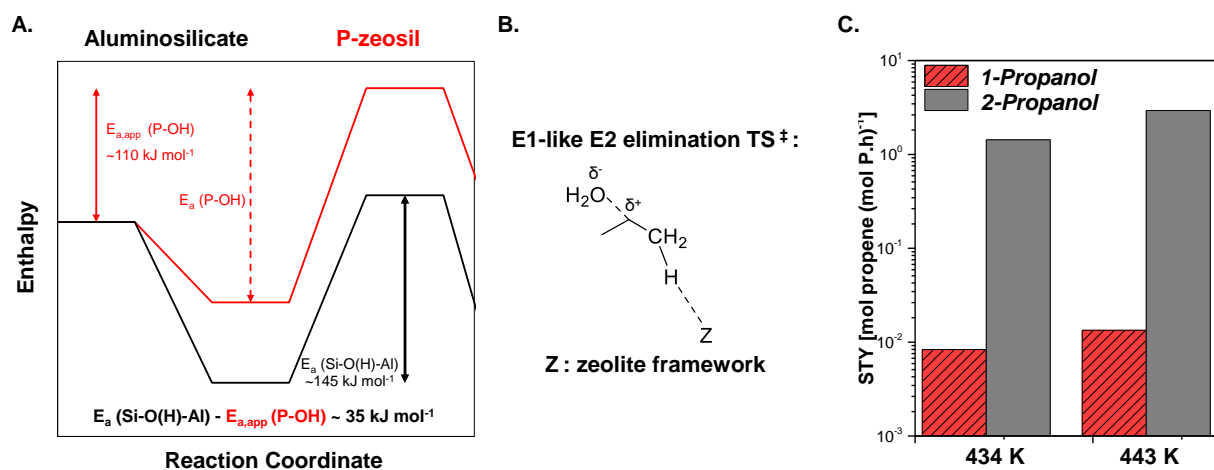


**Figure 4.** A. Proposed reaction coordinate diagram for the barriers on aluminosilicates (in black) and P-zeosils (in red). B. Illustration of proposed kinetically relevant transition state for the elimination pathway during unimolecular dehydration of 2-propanol. C. Propene site time yield measured on P-SPP using 1-propanol and 2-propanol feed at two temperatures (434 K, and 443 K) (Reaction conditions: WHSV = 2.5 – 2.9 g reactant g cat<sup>-1</sup> h<sup>-1</sup>, carrier gas (He) flowrate 25 sccm, conversions below 5%).



### 2.4.2. Nature of kinetically relevant transition state.

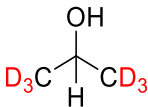
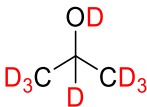
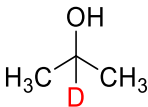
The rationalization for the seemingly contradictory apparent barriers assumes that while adsorption and reaction energetics may differ across the phosphorus containing- and aluminosilicate materials, the dehydration mechanism is unchanged and faces similar rate limiting step(s). To verify whether this assumption is reasonable, we investigated the kinetically relevant IPA dehydration step(s) with kinetic isotope effect (KIE) experiments involving deuterated alcohol reactants ( $C_3D_6(H)OH$ ,  $C_3D_7OD$ , and  $C_3H_6(D)OH$ ) (Table 3). Over P-SPP,  $C_3D_7OD$  exhibited a primary KIE of  $1.87 \pm 0.11$  for propene formation (Calculations included in Section S3.3 of SI), implicating the direct involvement of a X-H bond scission event in a kinetically relevant step. The analogous value with  $C_3D_6OH$  ( $1.63 \pm 0.05$ ) was relatively similar, suggesting that  $C_\beta-H$  cleavage is the only kinetically relevant X-H cleavage to propene formation. The absence of a KIE with a deuterated  $C_\alpha-H$  IPA feed ( $C_3H_6(D)OH$ ,  $1.07 \pm 0.06$ ) corroborates this conclusion, unambiguously identifying the  $C_\beta-H$  cleavage as a kinetically relevant step for propene formation.

These results are consistent with an E2-type elimination to propene, where  $C_\beta-H$  is not fully severed (in red, Figure 4B). Lercher and co-workers have reported similar KIE results in the case of secondary alcohols dehydration to olefins with aqueous-phase phosphoric acid.<sup>49,50</sup> While presence of solvent in these reports precludes a

direct comparison, our results are in qualitative agreement in that the  $C_\beta-H$  cleavage rate constant appears in the unimolecular dehydration kinetic expression.<sup>49,50</sup> It is important to note that ‘true’ E2 elimination (concerted single-step) does not result in the formation of a carbenium ion transition state, and it is reasonable to expect that the stability of the resulting carbenium would not affect unimolecular dehydration rates. However, a more than two order of magnitude increase in the rate of propene formation over P-SPP was observed using isopropanol compared to 1-propanol under identical reaction conditions (Figure 4C), suggesting that the mechanism is not truly a concerted E2 elimination. E2 elimination can often be complex, owing to possible asynchronous breaking combinations of  $C_\alpha-O$  and  $C_\beta-H$ , and leading to multiple possible transition states with varying degree of bond dissociation.<sup>47,48,53</sup> While a pure E2 elimination involves simultaneous severance of  $C_\alpha-O$  and  $C_\beta-H$ , an ‘E1-like’ E2 elimination in which breaking of the C-O bond is more pronounced than C-H, lends carbenium ion character to the unimolecular dehydration transition state; this would also corroborate an early transition state preserving the covalent  $C_\beta-H$  as evidenced by our KIE results.

Alternatively, KIE values for DIPE formation with  $CD_6OH$  ( $1.25 \pm 0.04$ ) and  $CD_7OD$  ( $1.09 \pm 0.10$ ) were significantly lower than those for propene, while  $C_3H_6(D)OH$  exhibited no KIE ( $1.03 \pm 0.13$ ) (Table 3). These secondary KIEs

**Table 3. Kinetic isotope effect with isopropanol, isopropanol (d8), isopropanol (d6) and isopropanol-d-OH on P-SPP (Si/P 30) and Al-MFI (Si/Al 140)**

Catalyst	$r_H/r_D$	Reactant		
				
P-SPP	Propene	$1.63 \pm 0.05$	$1.87 \pm 0.11$	$1.07 \pm 0.06$
	DIPE	$1.25 \pm 0.04$	$1.09 \pm 0.10$	$1.03 \pm 0.13$
Al-MFI	Propene	$1.71 \pm 0.18$	$1.82 \pm 0.07$	$0.43 \pm 0.03$
	DIPE	$1.16 \pm 0.15$	$1.13 \pm 0.03$	$0.47 \pm 0.02$

(Reaction conditions for P-SPP:  $T = 403\text{ K}$ ,  $P_{IPA} = 30\text{ torr}$ ,  $WHSV = 4.37\text{--}4.42\text{ g IPA g cat.}^{-1}\text{ h}^{-1}$ , Carrier gas (He) flowrate = 25 or 15 sccm; Conversions below 0.5%; Reactions for Al-MFI:  $T = 403\text{ K}$ ,  $P_{IPA} = 30\text{ torr}$ ,  $WHSV = 7.5\text{--}9.50\text{ g IPA g cat.}^{-1}\text{ h}^{-1}$ , Carrier gas (He) flowrate = 60 sccm; conversions below 2.2 %).

(Calculations included in Section S3.3 of SI) implicate an E1 elimination ( $C_{\alpha}$ -O scission) as the rate-limiting step for isopropanol (IPA) bimolecular dehydration. These results strongly suggest that unimolecular and bimolecular dehydration pathways proceed via distinct kinetically relevant activation events ( $C_{\beta}$ -H for uni-, and  $C_{\alpha}$ -O for bi-molecular dehydration) on P-SPP, which also explains the distinct apparent activation barriers of these pathways measured on all phosphorous containing materials.

We next compared KIE results across the two classes of materials to gauge potential differences in surface dehydration mechanisms. Measured KIE values for  $CD_6OH$  ( $1.71 \pm 0.18$ ) and  $CD_7OD$  ( $1.82 \pm 0.07$ ) over Al-MFI were found to be within experimental error of those on P-SPP (Figure 5), signaling similar rate determining constraints over the bridging hydroxyls of aluminosilicate and Brønsted acid sites of phosphorous containing materials. Conversely, an inverse KIE was observed with  $C_{\alpha}$ -H deuterated IPA ( $C_3H_6(D)OH$ ), both for the rate of propene ( $0.43 \pm 0.03$ ) and DIPE

formation ( $0.47 \pm 0.02$ ) (Table 3) on Al-MFI. This is an interesting result given we do not see any KIE with this  $C_{\alpha}$ -H deuterated feed on P-SPP (Table 3), suggesting that the coverage of a pre-equilibrated species is relevant, such that the measured KIE has significant thermodynamic contribution built into it. Specifically, we believe that deuterium substitution on the  $\alpha$ -carbon of IPA stabilizes the intermediate participating in the kinetically relevant transition state, resulting in a thermodynamic effect that dominates the overall rate constants ( $k_{TS}K_{ads}$ ) measured during KIE experiments. As to why inverse KIEs are observed on Al-MFI and not P-SPP, one needs to consider how the coverages at which these measurements are performed compare between the two materials. As noted before (Sec. 2.4.1), under identical conditions, surface coverages are significantly different on Al-MFI as compared with P-SPP; this is corroborated by lower apparent dehydration barriers observed on the P-zeosils on account of lower coverages. Mavrikakis and co-workers recently highlighted that thermodynamic isotope effect (TIE) values for

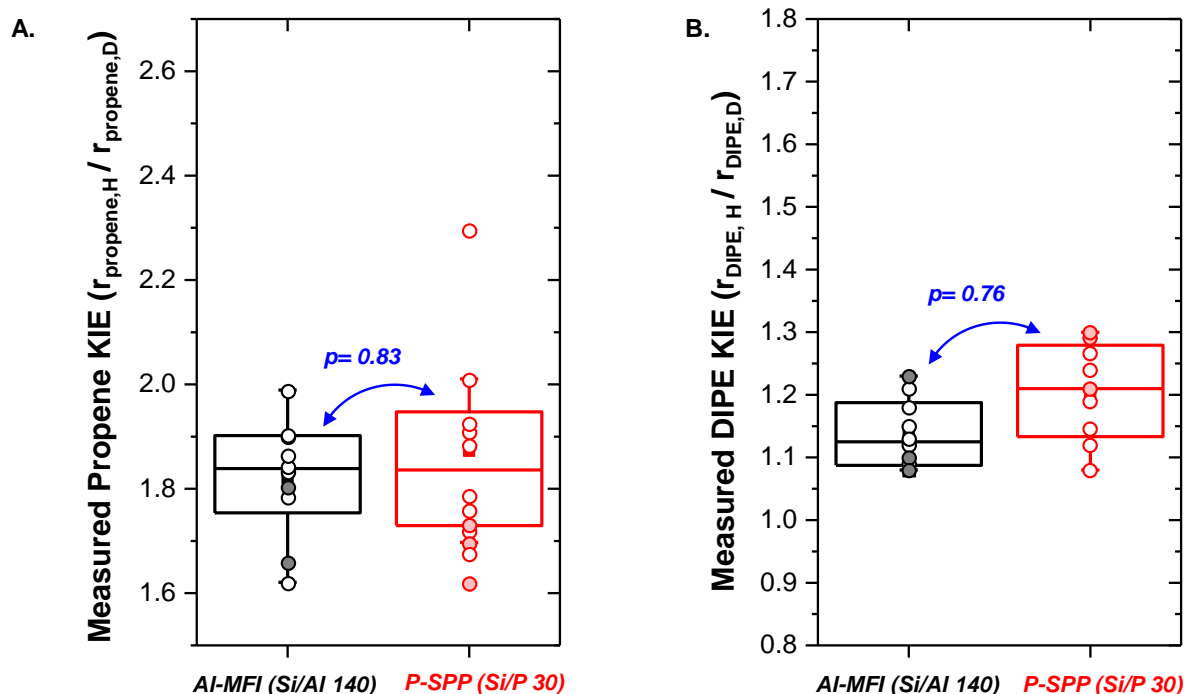


**Figure 5** A. Measured propene KIE on P-SPP compared with Al-MFI (Si/Al 140); B. Measured DIPE KIE on P-SPP compared with Al-MFI (Si/Al 140). The unfilled symbols correspond to IPA-d8, while the filled symbols are with IPA-d6. Analysis of variance was performed on the multiple replicates in each dataset and reported p-values (in blue) are reported at a 95% confidence interval. p-Values > 0.05 for both propene and DIPE indicate statistical insignificance between the KIE datasets reported on Al-MFI and the P-SPP.

H<sub>2</sub>/D<sub>2</sub> dissociative adsorption on transition metals decrease in absolute value with increasing surface coverages as the lateral interactions between adsorbates are highly coverage-dependent.<sup>54</sup> Based on these results, we believe that the difference in KIEs observed with C<sub>α</sub>-H deuterated IPA (C<sub>3</sub>H<sub>6</sub>(D)OH) between the two different materials once again captures coverage-related consequences to equilibrium constants.

Taken together, our KIE data highlight that the dehydration mechanism does not change between P-sites and Al-sites, and the differences noted in dehydration kinetics in this report reflect the implications of altered relative adsorption energetics rather than changes in dehydration mechanism.

**2.4.3. Effects of P-active site in isopropanol dehydration kinetics.** Olefin formation rates on aluminosilicate zeolites and polyoxometalates are typically inhibited at higher alcohol partial pressures irrespective of alcohol identity, due to the higher stability of adsorbed alcohol dimeric species relative to adsorbed monomers.<sup>37,39</sup> Macht et al. calculated this difference in the adsorption enthalpies to be ~84 kJ mol<sup>-1</sup> for 2-butanol on H<sub>3</sub>PW/SiO<sub>2</sub>,<sup>39</sup> while Zhi et al. measured it to be ~66 kJ mol<sup>-1</sup> for 1-propanol on Al-MFI.<sup>55</sup> While the expected inhibition of olefin formation at higher IPA partial pressure was observed over aluminosilicates (**Figure S13**), it was absent over phosphorous containing materials; near zero-order behavior ( $0.17 \pm 0.01$ ) was observed on P-SPP and P-BEA across a similar range of IPA partial pressure (**Figure 6A**). The lack of inhibition suggested a smaller difference between adsorption enthalpies of monomeric and dimeric IPA species on the active P-sites compared to aluminosilicates; surface-bound DIPE (DIPE\*) is not significantly more stable than surface bound IPA (IPA\*) on active P-sites. Indeed, adsorption energy calculations on P-SPP (**Figure 7**) revealed a marginal preference for DIPE adsorption over IPA (15 kJ mol<sup>-1</sup>), in stark contrast with the 61 kJ mol<sup>-1</sup> difference in the adsorption energy of DIPE and IPA on an aluminosilicate BAS (**Table 2**). Thus, a relatively destabilized DIPE\* results in the absence of inhibition in propene formation rates at higher IPA partial pressures over P-zeosils. It is instructive to note that zero-order propene

formation routes on P-SPP is not at odds with the earlier discussion of reported apparent barriers being measured from gas-phase reference state. While numerous early studies on alcohol dehydration considered the dimeric species as inert, more recent reports have highlighted the prevalence of olefin formation routes from the decomposition of adsorbed dimer.<sup>40,44,45</sup> It follows that the formation routes of olefin and di-alkyl ether can be coupled, and near zero-order propene formation behavior on P-SPP and P-BEA cannot directly be interpreted as evidence for a saturated surface.

To probe whether the propene and DIPE formation routes are coupled, DIPE was fed to the reactor under identical conditions to IPA dehydration on P-SPP. Relative to the propene formation rates from IPA, propene rates from DIPE were ~1.7x higher on P-SPP. While this increase is significantly smaller than over Al-MFI (where we observed a ~ 37x increase), these results suggest that there exists a pathway from DIPE to propene on P-SPP. To further probe the prevalence of this pathway, experiments were designed with IPA and DIPE cofeeds with molar IPA:DIPE ratios anticipated to mimic surface coverages during IPA dehydration (**Figure 6B**). Notably, changing the DIPE surface coverages could be used to alter propene formation rates (relative rates in the range of ~ 0.8-1.2 depending on IPA: DIPE molar ratios), and these data provide no evidence to support the claim that propene formation only results from IPA on P-SPP, thus elucidating the apparent nature of kinetic measurements on P-zeosils despite near zero-order reaction orders; propene originating from DIPE\* can mask the propene rate-order dependencies to appear close to zero-order even in a case where surface is relatively bare. Alternatively, DIPE formation rates were found to monotonically increase with IPA partial pressures on P-SPP and P-BEA (**Figure 6A**) with rate orders close to unity ( $0.70 \pm 0.01$ , and  $0.67 \pm 0.03$  on P-SPP and P-BEA, respectively).

The results of IPA dehydration, taken together, emphasize a recurring theme: the dehydration mechanism and the corresponding kinetically relevant steps remain unchanged across the two families of materials. Pathways for unimolecular and bimolecular dehydration are coupled on both materials, and the preference towards unimolecular

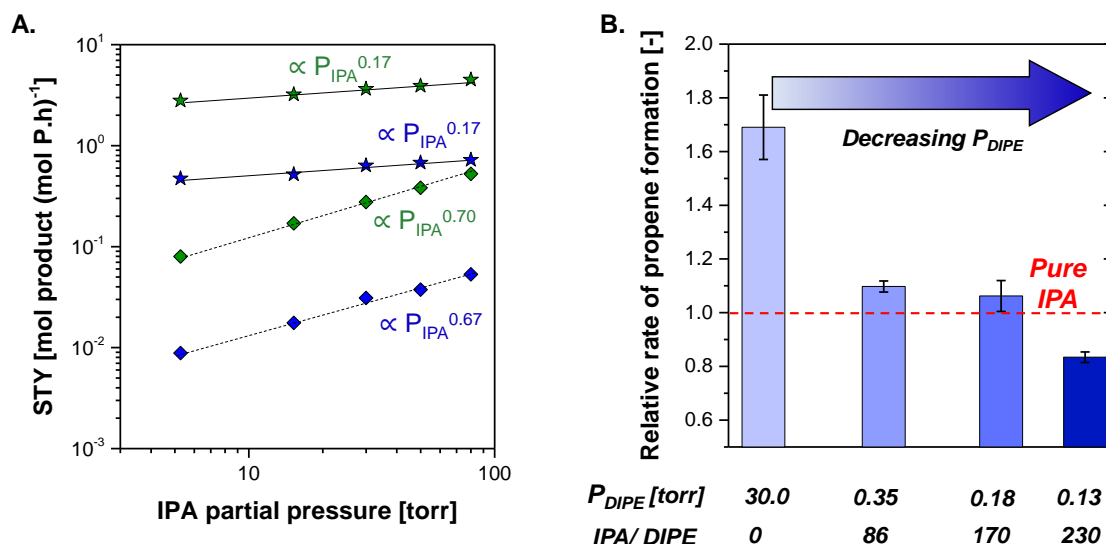


**Figure 6 A.** Propylene (★) and di-isopropyl ether (◆) synthesis rates as a function of IPA partial pressures measured on P-SPP (green) and P-BEA (blue) (Reaction conditions:  $T = 443$  K;  $\text{WHSV} = 2.5$  g reactant g cat<sup>-1</sup> h<sup>-1</sup>; Carrier gas (He) flowrate = 25 sccm; Conversions below 1.5%). Solid and dashed black lines indicate fits to IPA power-law rate expression for propene, and DIPE, respectively. The resulting IPA rate orders for both products are indicated for P-SPP (green) and P-BEA (blue); **B.** Relative rate of propene formation on P-SPP normalized to the corresponding value with IPA feed as a function of the molar ratio of IPA/DIPE during co-feed experiments (Reaction conditions:  $T = 403$  K,  $P_{\text{IPA}} = 30$  torr,  $\text{WHSV} = 3.1 - 5.3$  g reactant g cat<sup>-1</sup> h<sup>-1</sup>, carrier gas (He) flowrate 25 sccm, conversions below 0.4 %).

dehydration increases with temperature on both. The key difference between the two materials is a consequence of the differences in adsorption energies on their surfaces; the comparable stability of DIPE\* and IPA\* on P-active sites leads to an increased selectivity to propene as a dehydration product. For the same reason, inhibition of propene formation at higher IPA partial pressures is not readily observed with P-zeosils as it is over aluminosilicates. Ultimately, these differences manifest in markedly lower apparent activation energies on P-zeosils, despite the lower absolute rates of dehydration.

**2.4.4. Probing the P-sites by in-situ pyridine titration during IPA dehydration.** Given the *ex-situ* nature of the preceding measurements to probe P-zeosils discussed so far, we additionally evaluated the active sites of P-SPP and Al-SPP under isopropanol dehydration reaction conditions through *in-situ* titration methods. This allows us to more readily compare the intrinsic activity of aluminosilicates and P-active sites, accounting for sites actually involved in catalysis.<sup>56</sup> For acid

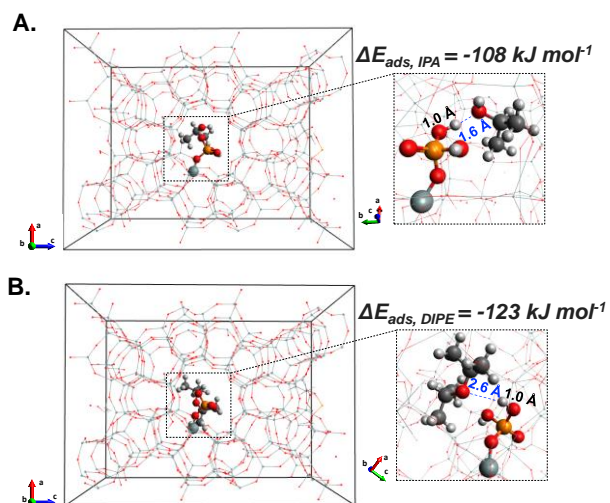


**Figure 7.** The optimized structures of **A.** IPA and **B.** DIPE on a P-active site. Adsorption energies corresponding to each case is indicated on the inset. The O-H atomic distances between the oxygen of adsorbate and the proton of P-active site are shown in blue and the O-H distances between the oxygen and hydrogen of the P-active site are shown in black.

catalysis (including alcohol dehydration<sup>6,24,57</sup>) on medium-pore microporous materials and larger, pyridine is the most commonly used *in-situ* titrant.<sup>58,59</sup> Assuming each pyridine molecule adsorbs on one acid site, the slope (rate vs mol pyridine uptake) and x-intercept (mol pyridine uptake) of the titration profile provide a measure of the STY and active site density under reaction conditions, respectively. Over a high silica Al-SPP (Si/Al 62), IPA dehydration mass-normalized rates dropped to >96% of their initial value upon pyridine saturation at 373 K, indicating that virtually all catalytic sites relevant to IPA dehydration had been titrated (**Figure 8A**). Pyridine partial pressures (11-120 mtorr) neither changed the measured STY nor BAS counts on Al-SPP (**Figure 8B**), and these values remain  $\sim 2.1$  mol mol  $\text{H}^+_{\text{py}}^{-1} \text{h}^{-1}$  and  $165 \mu\text{mol g}^{-1}$  at 373 K, respectively. Once pyridine is removed from the feed stream, dehydration rates do not recover (**Figure 8C**); pyridine remains irreversibly adsorbed on the active sites in Al-SPP. We then used three different IPA rate-normalization criteria: (i)

BAS counts assuming all the aluminum present in Al-SPP is active ( $265 \mu\text{mol g}^{-1}$ ), (ii) the BAS count measured during tBA Hofmann elimination of ( $190 \mu\text{mol g}^{-1}$ ),<sup>25</sup> and (iii) BAS counts obtained from the *in-situ* pyridine titration data ( $165 \pm 3 \mu\text{mol g}^{-1}$ ), to estimate errors in STYs arising from using these different criteria (**Figure 8D**). Assuming that all aluminum in Al-SPP is active leads to an underestimate of the STY; not all aluminum will tetrahedrally coordinate within the SPP framework and form a BAS. Regardless, all STY values remain within a factor of  $\sim 1.5$  of each other, meaning that different rate-normalization criteria only result in the minimal change in STY values for Al-SPP catalyst.

Over P-SPP, a more complex *in-situ* titration profile developed. As pyridine adsorbed on the active sites, IPA conversion rates dropped to  $\sim 75\%$  of their initial value under low pyridine partial pressures (5.4-6.6 mtorr). Increased pyridine concentrations in the feed led to both an increased degree of rate quenching, as well as the number of

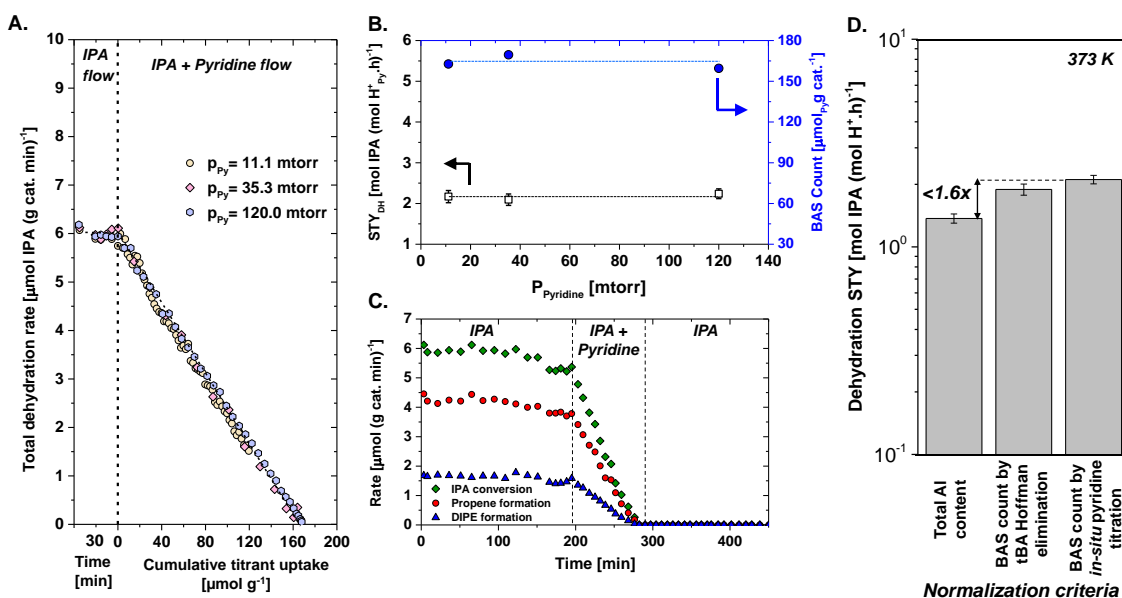


**Figure 8.** **A.** Mass-normalized IPA conversion rates plotted as a function of pyridine uptake during *in-situ* pyridine titration on Al-SPP at different pyridine partial pressures (in the range 5.4-101.3 mtorr). (Reaction conditions:  $T = 373$  K;  $P_{\text{IPA}} = 5.9$  torr;  $\text{WHSV} = 2.47$  g reactant g cat. $^{-1} \text{h}^{-1}$ ; Carrier gas (He) flowrate = 100 sccm; Conversions below 2%); **B.** (*primary axis*) IPA dehydration site time yields (STYs) as calculated by normalizing rates by cumulative pyridine uptake as a function of pyridine partial pressures, and (*secondary axis*) BAS count assuming a 1:1 stoichiometry between cumulative pyridine uptake and BAS; **C.** Mass-normalized rates of IPA conversion ( $\blacklozenge$ ), propene formation ( $\bullet$ ) and DIPE formation ( $\blacktriangle$ ) as a function of time-on-stream (TOS). (Reaction conditions: IPA: Pyridine 530:1, while other conditions are identical to (A) and (B)); **D.** Site time yield of IPA dehydration calculated with different normalization criteria. Error bars are standard errors calculated by propagation of relative errors in mass-normalized rate and total acid site counts used for normalization.



acid sites counted. The rate suppression increased from ~75% to ~87% due to a twenty-fold increase in pyridine partial pressure (5.4 to 101.3 mtorr). Acid site counts, as obtained by extrapolation of the linear region of the rate versus cumulative uptake traces, also increased from 40 to 126  $\mu\text{mol g}^{-1}$ . The non-zero rate of dehydration at pyridine saturation, combined with the effect of increasing pyridine partial pressure, present a possibility that P-sites capable of catalyzing isopropanol (IPA) conversions do not bind pyridine irreversibly. Given the catalytic site heterogeneity,<sup>8,17</sup> it is also plausible that higher concentrations of pyridine titrated 'less-reactive' sites, leading to higher acid site counts. However, we find this possibility unlikely given that propene and di-isopropyl ether (DIPE) selectivities remain nearly invariant with pyridine partial pressure after saturation (**Figure S12 in Section S3.2 in the SI**). It is improbable that multiple inequivalent active sites would turnover IPA in a manner that preserves an identical unimolecular/dehydration pathway selectivity. It is

more likely that the pyridine partial pressure dependence of acid site counts results from competitive adsorption between IPA and pyridine. From **Figure 9A and B**, we note that the slopes change with pyridine partial pressure and the quantification of a unique STY value is challenging. To further add to the complications involving STY measurements, although these active sites do bind pyridine, they do so reversibly; upon pyridine removal from the feed stream, both propene and DIPE rates start recovering on time-scales of minutes (**Figure 9C**). Given that infinitely small pyridine uptakes are more representative of strict chemisorption on P-active sites, we believe that the most accurate turnover frequency is the value extrapolated to zero pyridine partial pressures, which results in a STY of 2.2  $\text{mol mol H}^+_{\text{py}}^{-1} \text{ h}^{-1}$  at 403 K (**Figure 9B**). Similar analysis for the cumulative pyridine uptakes further allows for an estimation of acid site counts as 40  $\mu\text{mol g}^{-1}$ , which is generally in reasonable agreement with the BAS counts obtained during Hofmann elimination of

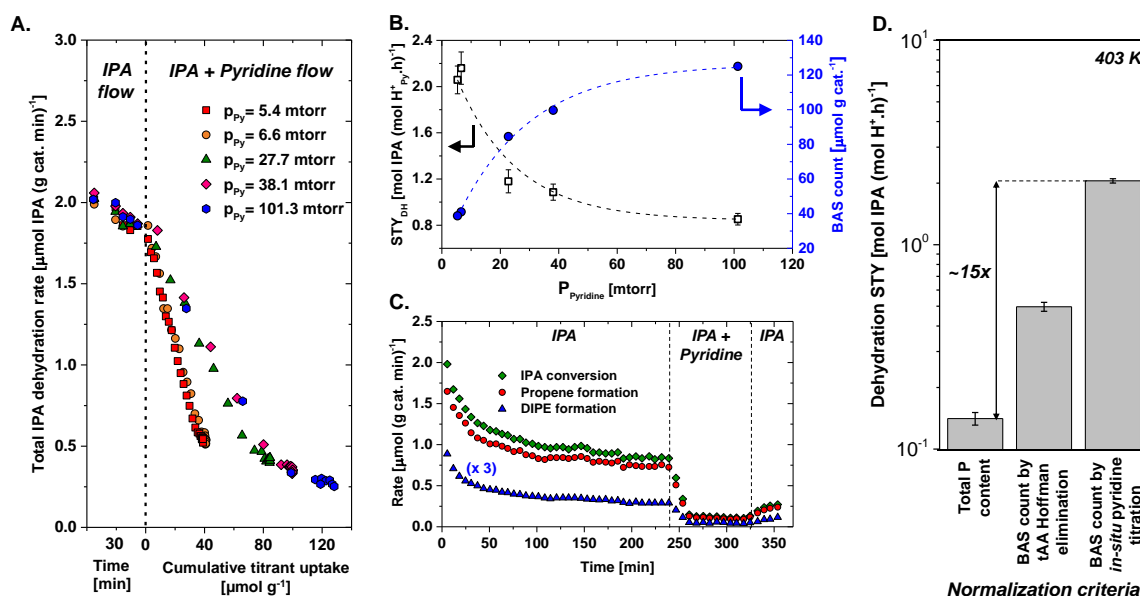


**Figure 9.** A. Mass-normalized IPA conversion rates plotted as a function of pyridine uptake during in-situ pyridine titration on P-SPP at different pyridine partial pressures (in the range 5.4-101.3 mtorr). (Reaction conditions:  $T = 403 \text{ K}$ ;  $P_{\text{IPA}} = 30 \text{ torr}$ ;  $\text{WHSV} = 2.59 \text{ g reactant g cat}^{-1} \text{ h}^{-1}$ ; Carrier gas (He) flowrate = 25 sccm; Conversions below 0.5%); B. (primary axis) IPA dehydration site time yields (STYs) as calculated by normalizing rates by cumulative pyridine uptake as a function of pyridine partial pressures, and (secondary axis) BAS count assuming a 1:1 stoichiometry between cumulative pyridine uptake and BAS; C. Mass-normalized rates of IPA conversion ( $\blacklozenge$ ), propene formation ( $\bullet$ ) and DIPE formation ( $\blacktriangle$ ) as a function of time-on-stream (TOS) (Reaction conditions: IPA: Pyridine 780:1, while other conditions are identical to (A) and (B)); D. Site time yield of IPA dehydration calculated with different normalization criteria. Error bars are standard errors calculated by propagation of relative errors in mass-normalized rate and total acid site counts used for normalization.

isopropyl amine ( $46 \mu\text{mol g}^{-1}$ ), albeit lower than more reactive alkylamines like tBA and tAA (Figure 1A).

As shown in Figure 9D, STY values vary by  $\sim 15\times$  depending on the normalization criteria used, which is a direct consequence of the low number of protons per heteroatom ( $\text{H}^+/\text{P}_{\text{bulk}} \sim 0.1\text{-}0.2$ ) counted by the two site-counting methods employed (Hofmann elimination and *in-situ* pyridine titration). We note that similar proton/heteroatom values have been previously reported on other weakly Brønsted acidic materials (e.g.  $\text{H}^+/\text{X}_{\text{bulk}}$  in the range  $\sim 0.1\text{-}0.25$  for B-MFI)<sup>5,6</sup> and it follows from the discussion that a majority of phosphorus in P-SPP is inactive for IPA dehydration/Hofmann elimination chemistries. However, within the limitations of this technique, this analysis allows for a reasonable comparison of phosphorous containing materials and aluminosilicate per active site. At 403 K, total dehydration STY for Al-SPP is  $17.6 \text{ mol H}^+_{\text{py}}^{-1} \text{ h}^{-1}$  (Table 1), while it is almost an order of magnitude lower on P-SPP ( $2.2 \text{ mol H}^+_{\text{py}}^{-1} \text{ h}^{-1}$ ) (Table 1 and Figure 9D).

**3. Conclusion.** This report probes the active sites in phosphorus-containing zeosils during Brønsted acid catalysis. Site-counts as obtained by Hofmann elimination of alkylamines demonstrate that more reactive tertiary alkylamine feeds (e.g., tert-amylamine) can carry out olefin formation turnovers on more active sites than primary alkylamines (e.g., n-propylamine) – a finding in sharp contrast to aluminosilicates where amine identity does not change the number of sites involved in olefin formation. During IPA dehydration, these P-zeosils exhibit  $> 80\times$  lower heteroatom-normalized turnover rates than aluminosilicates, which is indicative of lower inherent activity of active sites and/or the presence of catalytically inactive P-species. Furthermore, these materials show a clear kinetic preference to unimolecular dehydration routes, yielding 20-30% higher propene selectivities than aluminosilicate analogs under identical reaction conditions. A diminished difference between adsorption energies of IPA and DIPE allows propene rates to remain uninhibited at high IPA partial pressures. IPA dehydration to propene is found to proceed through an E2-elimination route with kinetically relevant

$\text{C}_\beta\text{-H}$  scission on P-SPP. More importantly, the dehydration mechanism remains unaltered from the aluminosilicates, highlighting that differences in reaction performance are direct implications of weaker binding to active sites in P-zeosils. This weaker binding further affords an apparent lowering of lower uni-/bimolecular dehydration barriers by  $\sim 35 \text{ kJ mol}^{-1}$  compared to aluminosilicates.

## 4. Materials and methods

### 4.1 Materials Synthesis and Characterization.

The following were purchased and used without any further treatment: Isopropanol (anhydrous,  $\geq 99.5\%$ , Sigma Aldrich), Isopropanol-d<sub>6</sub> (99 atom%, Sigma Aldrich), Isopropanol-d<sub>8</sub> ( $\geq 99.5$  atom%, Sigma Aldrich), Isopropanol D(OH) ( $> 98\%$ , Sigma Aldrich), 1-propanol (anhydrous,  $\geq 99.7\%$ , Sigma Aldrich), Ethanol (200 proof,  $\geq 99.5\%$ , Sigma Aldrich), Di-isopropyl ether ( $> 99\%$  with BHT as stabilizer, Sigma Aldrich), Pyridine (99.8 %, Sigma Aldrich), n-Propylamine ( $\geq 99\%$ , Sigma Aldrich), n-Butylamine ( $\geq 99.5\%$ , Sigma Aldrich), Isopropylamine ( $\geq 99.5\%$ , Sigma Aldrich), Cyclopentylamine (99%, Sigma Aldrich), Tert-butylamine ( $\geq 99.5\%$ , Sigma Aldrich), Tert-amylamine ( $\geq 98\%$ , Sigma Aldrich), 2,6-di-tert-butyl pyridine (DTBP,  $\geq 97\%$ , Sigma Aldrich), Phosphoric acid (85 wt%, Sigma Aldrich), Tetra(n-butyl)phosphonium hydroxide (TBPOH 40 wt%, TCI America), Tetraethyl orthosilicate (TEOS, 98%, Sigma-Aldrich), Hydrochloric acid (37wt%, Sigma Aldrich), Cetyltrimethylammonium chloride (CTAB,  $\geq 98\%$ , Sigma-Aldrich), Tetrapropylammonium bromide (TPABr, 98%, Sigma Aldrich), Hydrofluoric acid (48 wt% aqueous solution, Sigma Aldrich), Fumed silica (Cab-o-sil M5, scintillation grade, Acros Organics), PEO-PPO-PEO (P123, Sigma-Aldrich), Silicon-dioxide (quartz chips, 4-20 mesh, Sigma Aldrich), Tetrapropylammonium hydroxide (TPAOH 40 wt% in water, Alfa Aesar), Tetraethylammonium hydroxide solution (TEAOH, 40 wt % in water, Sigma Aldrich), Tetraethyl orthosilicate (TEOS,  $\geq 99\%$ , Sigma Aldrich).

Ammonium form ZSM-5 (CBV 8014, Si/Al 40), ZSM-5 (CBV28014, Si/Al 140), and Al-BEA

(CP814C, Si/Al 12.5) were obtained from Zeolyst International. Al-SPP (Si/Al 62) was the same sample previously characterized and reported by Xu *et al.*<sup>25</sup> P-zeosils (P-SPP, P-BEA, P-MFI, P-SBA-15, P-MCM-41, P-Stöber) were synthesized by post-synthetic modification of all-silica analogues with an intended phosphorus loadings of Si/P molar ratio ~30, and detailed synthesis protocols can be found in the supporting information (**Section S.1**). All catalysts were calcined in a boat placed within a 1" quartz tube under air flow at 823 K using a ramp rate of 2 K min<sup>-1</sup> for 10 hours prior to any catalytic testing.

Powder X-ray diffraction (XRD) patterns were collected on a Bruker AXS D5005 diffractometer using Cu K $\alpha$  radiation ( $\lambda$  = 1.5418 Å) with a step size of 0.02° and a step time of four seconds. Inductively Coupled Plasma Optical Emission Spectrometry (ICP-OES) (Galbraith Laboratories) was used for elemental analysis of silicon and phosphorus for all reported catalysts. Textural characterization of all synthesized samples was performed with Ar physisorption in an Autosorb iQ2 porosimetry instrument (Quantachrom). Prior to analysis, crushed catalyst powders were outgassed at 573 K for six hours and subsequently cooled down to room temperature under vacuum. Brunauer–Emmett–Teller (BET) specific surface area measurements were used to represent the total surface area of the catalyst materials, and total pore volume was determined at  $P/P_0 = 0.95$  for SPP, BEA, and MFI, and  $P/P_0 = 0.99$  for SBA-15, Stöber, and MCM-41. Scanning electron microscopy (SEM) was performed on a JEOL JSM-6500F scanning microscope operated at 5.0 kV.

Infrared (IR) spectra for pyridine were collected for P-SPP and Al-SPP on a Nicolet iS50 Fourier-transform infrared spectroscopy (FTIR) spectrometer with a Hg-Cd-Te (MCT, cooled to 77 K by liquid N<sub>2</sub>) detector in the 4000 – 600 cm<sup>-1</sup> range and were taken relative to an empty cell background reference collected under dynamic vacuum (< 0.01 Torr) at 423 K. Self-supporting wafers (10 -15 mg/cm<sup>2</sup>) were sealed within an IR transmission cell (Harrick Scientific, ATK-024-3) with ZnSe windows. Wafer temperatures were measured within 2.0 mm of each side of the wafer by type K thermocouples (Omega). The IR cell was connected to a glass vacuum manifold, used for exposing the catalyst sample to controlled amounts

of pyridine vapor. The catalyst sample was pretreated in-situ at 673 K for five hours with a ramp of 2.0 K min<sup>-1</sup>, then cooled down to 423 K where pyridine was dosed until saturation. Finally, the temperature was raised to 623 K with a rate of 1.0 K min<sup>-1</sup> while simultaneously collecting spectra every 3.0 min (Scan resolution of 4.0 cm<sup>-1</sup>, total number of scans = 128).

**4.2 Active Site Quantification.** Brønsted acid site (BAS) densities for all aluminosilicates reported in this work (Al-SPP, Al-MFI, and Al-BEA) were probed using the Hofmann elimination of tert-butylamine. To probe P-zeosils, Hofmann elimination of alkylamines with varying proton affinities (n-propylamine, n-butylamine, isopropyl amine, cyclopentylamine, tert-butylamine, tert-amylamine)<sup>28</sup> was performed and compared with analogous experiments with Al-MFI (Si/Al 140). All of these measurements were performed on a custom-made reactive gas chromatography (RGC) setup which essentially condenses a typical temperature-programmed desorption mass spectrometer (TPD-MS) within a gas chromatograph; the fabrication of the setup are detailed in Abdelrahman *et al.*<sup>28</sup>.

Catalysts were pelletized and sieved to load ~ 20-30 mg of sample (500-1000  $\mu$ m fraction), placed between plugs of deactivated quartz wool in a split inlet liner of the RGC setup. Samples were calcined *in-situ* in air at 673 K for one hour with a temperature ramp rate of 10 K min<sup>-1</sup>. Thereafter, the gas was switched to helium (He), and the liner was cooled down to 423 K, where it was held for 30 min prior to amine dosing. The probe amine was dosed as pulses using an automated liquid sampler (ALS), and saturation of the sample surface was ascertained by monitoring eluent amine breakthrough using a flame ionization detector (FID) directly downstream of the inlet. Once saturated, the bed was purged under a continuous stream of He (90 sccm) at the same temperature (423 K) for two hours to remove any physisorbed amine molecules. Thereafter, the temperature of the inlet liner was ramped from 423 K to 673 K at 10 K min<sup>-1</sup> and held there for 30 min allowing for the adsorbed alkylamine to either desorb intact or undergo a Hofmann elimination to corresponding olefin and ammonia, while holding the GC oven at 303 K to trap all eluting alkenes. At the end of 30

minutes at 673 K, the temperature of the GC column, containing the trapped molecules, was raised from 303 K to 543 K at a ramp rate of 10 K min<sup>-1</sup> and held there for 10 min to allow the olefin to elute from the column, and quantification was through the FID. A stoichiometry of 1:1 was assumed between the olefin and the BAS. These moles were normalized by the mass of sample loaded in the inlet liner to yield a Brønsted acid site mass density ( $\mu\text{mol BAS g cat.}^{-1}$ ).

TPD curves for the tert-butylamine Hofmann elimination as well as molecular desorption were simulated using the Polanyi-Wigner equation using the kinetic parameters obtained from steady-state kinetic measurements. Two additional assumptions were made in this analysis: i) there is complete coverage of BAS by tBA at the start of the TPD for both set of materials, and ii) pre-exponential factor and activation energy are not a function of coverage. An open-access MATLAB code for the simulated TPD is available.<sup>60</sup>

**4.3 Catalytic Experiments.** All kinetic measurements for isopropanol dehydration were performed for a range of partial pressure (3-100 torr) and temperatures (373 – 453 K) at ambient overall pressure in an upflow fixed bed reactor. While the majority of mechanistic studies were conducted on P-SPP, other P-zeosils were also probed to assess the support-dependence of active P-sites. Catalyst samples were pressed and sieved to particle aggregates of 106-250  $\mu\text{m}$  and placed between deactivated quartz wool plugs in a 1/4" quartz U-tube; catalyst masses were in the range 25-70 mg. Void volume in the tube was minimized by loading quartz chips upstream of the catalyst bed. A 1/16" type-K thermocouple (Omega) was placed just above the catalyst bed for temperature measurements, and isothermal conditions were ensured by housing the reactor in a resistively heated furnace (MTI Corporation, GSL-1100X) with temperature control (PID controller, Omega CN 7800). All catalyst samples were calcined *in situ* at 823 K in 40 sccm air (99.997%, Minneapolis Oxygen) using a temperature ramp rate of 5.0 K min<sup>-1</sup>. They were then cooled to reaction temperature and purged with He (99.995 %, Minneapolis Oxygen) for at least 30 minutes prior to the introduction of reactant feed.

Reactant partial pressures were kept in the range ~2-100 torr by varying the volumetric flowrate of the reactants using a syringe pump (Cole Parmer 74905 series), and/or carrier gas flowrates (15-100 sccm) by a mass flow controller (Brooks Instruments 5850E). Pressure drops across the catalyst beds were maintained below 10% of total pressure. All transfer lines were maintained at temperatures  $\geq 400$  K to avoid condensation of any species. All carbon atom balances closed to within ~5%. Online analysis of the reactor effluent was performed with gas-sampling injections using a gas chromatograph (Agilent 7890A) equipped with a quantitative carbon detector (QCD, Polyarc™)<sup>61</sup> and a flame ionization detector (FID), and separation was performed using an HP-PLOT Q column (Agilent, 19091P-QO4). To the extent possible, kinetic studies for a given synthesized catalyst were performed with the same batch for which all the characterization results are also reported (XRD, SEM, Ar-adsorption). In cases where kinetic data from multiple batches are reported, these batches were subjected to a reference catalytic condition (403 K, 30 torr IPA, WHSV of ~2.5 g IPA/ g cat./ h, 25 sccm diluent (He) flowrate) to assess any variations originating from synthesis procedures. All reported catalysis data are either from fully characterized batches or from batches that exhibit negligible variations (< 0.2% difference in conversions) in catalytic performance from the fully characterized batch at the reference condition specified above.

A combination of Mears' and Weisz-Prater criterion was used to ascertain the absence of external and internal mass transfer limitations, respectively (**Section S3.5 in the SI**).<sup>62</sup> All reported rates are initial rates ( $t=0$ ) under differential conversions (< 5% in all measurements for P-zeosils, and <10% for all measurements for aluminosilicates), which are obtained by correcting for intervening, albeit minor, catalyst deactivation under reaction conditions. For P-SPP catalyst, regeneration studies (re-calcining *in situ* at 823 K in 40 sccm air (99.997%, Minneapolis Oxygen) using a temperature ramp rate of 5.0 K min<sup>-1</sup>) were carried out to find that deactivation was reversible (**Section S.3.1 in the SI**). For all *in-situ* pyridine titration experiments, isopropanol dehydration was carried out until initial transients subsided, and an instantaneous switch was made to the IPA/titrant



mixture (molar ratio~250-5500) at identical volumetric flowrate. Experiments with multiple pyridine partial pressures were performed by varying the molar ratio of IPA : pyridine in the feed mixture. An identical methodology of instantaneous switch to deuterated IPA feeds allowed for the measurement of kinetic isotope effect values. Unless otherwise mentioned, error bars are reported at a 95% confidence level.

**4.4 Adsorption energy calculations using Density Functional Theory.** Calculations of molecular adsorption on the active P-site was modeled as a  $Q_1^1$  site with adjacent silanol (**Figure S7 in the Section S.2**). We note that there may be other possible Brønsted acidic -OH moieties in the wide variety of P-environments expected in these materials as noted in Jain et al.,<sup>17</sup> but we only consider the  $Q_1^1$  site for these simulations. Analogous calculations on the bridging hydroxyl BAS in aluminosilicate MFI were also carried out for comparison. Calculations on the surface of the MFI framework were performed using periodic density functional theory (DFT) with the Vienna Ab Initio Simulation Package (VASP)<sup>63</sup> version 6.1.0 incorporated in the MedeA Environment. The generalized gradient corrected Perdew-Burke-Ernzerhof (GGA-PBE)<sup>64</sup> exchange correlation functional was employed in all calculations with a plane-wave basis set and the projector augmented wave (PAW) potentials, where Si (3s3p), O (2s2p), P (3s3p), Al (3s3p), H (1s), C (2s2p), and N (2s2p) were included explicitly in the valence.<sup>65,66</sup> A cutoff of the plane-wave basis of 500 eV along with the  $\Gamma$ -point sampling of reciprocal space was used. DFT-D3 with Becke-Johnson (BJ) -damping was used to include van der Waals interactions between the adsorbate and zeolite.<sup>67,68</sup> A Gaussian smearing of 0.05 eV was applied at the Fermi level, and the total energies were extrapolated to zero smearing. Geometry optimizations were converged to an energy threshold of  $10^{-5}$  eV and a force threshold of  $0.02 \text{ eV } \text{\AA}^{-1}$ . Structure visualization was obtained using Avogadro<sup>69,70</sup> version 1.2.0.

An all-silicate MFI periodic unit cell ( $20.090 \times 19.738 \times 13.142 \text{ \AA}$ ,  $\alpha, \beta, \gamma = 90^\circ$ ) was obtained from the International Zeolite Association (IZA) database. The T12-site is the most frequently chosen site for aluminum substitution due to its presence at the interception of the straight and sinusoidal channels of MFI<sup>71-73</sup> and the lowest energy among all 12 T-sites,<sup>74,75</sup> T2-site is also

located at the interception of channels<sup>75,76</sup> and is energetically comparable to T12-site for aluminum incorporation.<sup>75</sup> Additionally, the energetically most favorable T-site for the P-active site is unknown. As such, calculations were performed and compared on both T2 and T12-sites for both set of sites (Al-, and P-) to choose the most representative T-site for adsorption energy calculations.

To construct an internal BAS, one silicon on the T12-site or T2-site was substituted by an aluminum atom. The resulting negative charge from aluminum incorporation on the oxygen of the Si-O-Al linkage was balanced by a proton to form an internal BAS, followed by a geometry optimization (**See Figure S.9 in Section S.2 for details**). Internal BAS on the T12-site was calculated to be  $13 \text{ kJ mol}^{-1}$  more stable than BAS on the T2-site, and was therefore chosen for adsorption energy calculations on aluminum-containing MFI. In an analogous manner, an internal P-active site was constructed by breaking the Si-O-Si linkage of a T2-site or T12-site silicon (**Figure S7 in Section S.2**), where a phosphoric acid was attached to generate the internal P-active site, while the other silicon previously on the Si-O-Si linkage was terminated as a silanol group, as shown with the P-active site on a T2-position in **Figure S7A (Section S.2)**. As the T2-site is close to the boundary of the unit cell in the c direction,  $1 \times 1 \times 2$  supercells were constructed using the optimized structures for clear visualization of the internal acid sites and the interactions with adsorbent molecules after structure optimizations in the  $1 \times 1 \times 1$  unit cell. Notably, the internal P-active site was found to be  $\sim 74 \text{ kJ mol}^{-1}$  more favorable on the T2-site compared to T12-site, indicating that while aluminum incorporation occurs on T12 position, P-active site is more likely to locate at the T2-site of MFI. Therefore, DFT calculations were performed on the T2-site for adsorption on P-active site.

Similarly, all adsorption energy calculations on the external surface of P-MFI were accomplished by constructing an external surface defined by a slab formed between two pentasil layers of MFI (**Figure S7B in Section S.2**).<sup>77</sup> The two pentasil layers were separated perpendicularly by a vacuum gap of  $20 \text{ \AA}$  to prevent interactions between the two layers. Vacuum slabs of  $10 \text{ \AA}$  were applied between the pentasil layers and the upper and bottom



boundaries of the periodic unit cell to prevent interactions between pentasil layers in adjacent periodic cells. The dangling Si-O bonds were terminated as silanol groups at the top and bottom surfaces of the pentasil layers.<sup>78</sup> An external P-active site was constructed by attaching a phosphoric acid on the T2-site with the same method used to construct the internal P-active site (**Figure S7B in Section S.2**). A structural optimization was then performed on the structure containing an external P-active site at the T2 position.

Prior to adsorption calculations, probe molecules including tert-butylamine, IPA, and DIPE were optimized separately in a  $25 \times 25 \times 25$  Å cell. The energy-minimized molecules were then loaded to the zeolite unit cell with the oxygen of IPA and DIPE and the nitrogen of tert-butylamine facing the proton of Al- or P-active site. The initial N-H or O-H distances between the adsorbate nitrogen or oxygen and acid site proton were close to one bond length of the O-H bond in Al-, or P-active site. All atomic positions and lattice constants were relaxed to obtain adsorption structures. The adsorption energy ( $\Delta E_{\text{ads}}$ ) was calculated,

$$\Delta E_{\text{ads}} = E_{\text{ZA}} - E_{\text{Z}} - E_{\text{A}} \quad (1)$$

where  $E_{\text{Z}}$  and  $E_{\text{A}}$  are the minimized electronic energy of the zeolite framework and adsorbate, respectively, while  $E_{\text{ZA}}$  is the minimized electronic energy of the final adsorption structure.

**Acknowledgements.** We acknowledge support from the Catalysis Center for Energy Innovation, an Energy Frontier Research Center funded by the U.S. Department of Energy, Office of Science, Office of Basic Energy Sciences under Award number DE-SC0001004. We acknowledge Dr. Xuekui Duan (UMN) for obtaining SEM images of all catalysts reported, and Dr. Dandan Xu (UMass Amherst) for providing the Al-SPP sample. We also thank Dr. Manish Shetty (UMN) and Dr. Alexander M. Ardagh (UMN) for helpful technical discussions.

**Supporting Information.** Details of all synthesis procedures followed, PXRD, SEM, Ar-sorption data for all synthesized P-zeosils, optimized

structures for all adsorption energy calculations, details of catalytic evaluation of P-zeosils and aluminosilicates during IPA dehydration, as well as the assessment of external and internal transport limitations.

**Keywords.** phosphorus-zeosils, dehydration, Hofmann elimination, isopropanol, propene, diisopropyl ether, Brønsted acidity

## References.

- (1) Walker, T. W.; Motagamwala, A. H.; Dumesic, J. A.; Huber, G. W. Fundamental catalytic challenges to design improved biomass conversion technologies. *J. Catal.* **2019**, *369*, 518–525.
- (2) Climent, M. J.; Corma, A.; Iborra, S. Conversion of biomass platform molecules into fuel additives and liquid hydrocarbon fuels. *Green Chem.* **2014**, *16* (2), 516–547.
- (3) Serrano, D. P.; Melero, J. A.; Morales, G.; Iglesias, J.; Pizarro, P. Progress in the design of zeolite catalysts for biomass conversion into biofuels and bio-based chemicals. *Catal. Rev. - Sci. Eng.* **2018**, *60* (1), 1–70.
- (4) Simonetti, D. A.; Dumesic, J. Catalytic production of liquid fuels from biomass-derived oxygenated hydrocarbons: Catalytic coupling at multiple length scales. *Catal. Rev. - Sci. Eng.* **2009**, *51* (3), 441–484.
- (5) Kumar, G.; Liu, D.; Xu, D.; Tsapatsis, M.; Dauenhauer, P. J.; Page, S. Dehydration-Decyclization of 2-Methyltetrahydrofuran to Pentadienes on Boron-Containing Zeolites. *Green Chem.* **2020**, *22*, 4147–4160.
- (6) Jones, A. J.; Carr, R. T.; Zones, S. I.; Iglesia, E. Acid strength and solvation in catalysis by MFI zeolites and effects of the identity, concentration and location of framework heteroatoms. *J. Catal.* **2014**, *312*, 58–68.
- (7) Abdelrahman, O. A.; Park, D. S.; Vinter, K. P.; Spanjers, C. S.; Ren, L.; Cho, H. J.; Zhang, K.; Fan, W.; Tsapatsis, M.; Dauenhauer, P. J. Renewable Isoprene by Sequential Hydrogenation of Itaconic Acid

- and Dehydra-Decyclization of 3-Methyl-Tetrahydrofuran. *ACS Catal.* **2017**, 7 (2), 1428–1431.
- (8) Cho, H. J.; Ren, L.; Vattipalli, V.; Yeh, Y.-H.; Gould, N. G.; Xu, B.; Gorte, R. J.; Lobo, R.; Dauenhauer, P. J.; et al. Renewable p-Xylene from 2,5-Dimethylfuran and Ethylene Using Phosphorus-containing Zeolite Catalysts. *ChemCatChem* **2017**, 9, 398-402.
  - (9) Abdelrahman, O. A.; Park, D. S.; Vinter, K. P.; Spanjers, C. S.; Ren, L.; Cho, H. J.; Vlachos, D. G.; Fan, W.; Tsapatsis, M.; Dauenhauer, P. J. Biomass-Derived Butadiene by Dehydra-Decyclization of Tetrahydrofuran. *ACS Sustain. Chem. Eng.* **2017**, 5 (5), 3732-3736.
  - (10) Zhang, X.; Liu, D.; Xu, D.; Asahina, S.; Cychosz, K. A.; Agrawal, K. V.; Al Wahedi, Y.; Bhan, A.; Al Hashimi, S.; Terasaki, O.; et al. Synthesis of Self-Pillared Zeolite Nanosheets by Repetitive Branching. *Science* **2012**, 336 (6089), 1684–1687.
  - (11) Gulbinski, J.; Ren, L.; Vattipalli, V.; Chen, H.; Delaney, J.; Bai, P.; Dauenhauer, P.; Tsapatsis, M.; Abdelrahman, O. A.; Fan, W. Role of silica support in phosphoric acid catalyzed production of p-xylene from 2,5-dimethylfuran and ethylene. *Ind. Eng. Chem. Res.* **2020**, 59 (51), 22049–22056.
  - (12) Ipatieff, V.; Corson, B. B.; Egloff, G. Polymerization, a New Source of Gasoline. *Ind. Eng. Chem.* **1935**, 27 (9), 1077–1081.
  - (13) De Klerk, A.; Engelbrecht, D. J.; Boikanyo, H. Oligomerization of fischer-tropsch olefins: Effect of feed and operating conditions on hydrogenated motor-gasoline quality. *Ind. Eng. Chem. Res.* **2004**, 43 (23), 7449–7455.
  - (14) De Klerk, A.; Leckel, D. O.; Prinsloo, N. M. Butene oligomerization by phosphoric acid catalysis: Separating the effects of temperature and catalyst hydration on product selectivity. *Ind. Eng. Chem. Res.* **2006**, 45 (18), 6127–6136.
  - (15) Schwarzer, R.; du Toit, E.; Nicol, W. Solid phosphoric acid catalysts: The effect of free acid composition on selectivity and activity for 1-hexene dimerisation. *Appl. Catal. A Gen.* **2009**, 369 (1–2), 83–89.
  - (16) Krawietz, T. R.; Lin, P.; Lotterhos, K. E.; Torres, P. D.; Barich, D. H.; Clearfield, A.; Haw, J. F. Solid phosphoric acid catalyst: A multinuclear NMR and theoretical study. *J. Am. Chem. Soc.* **1998**, 120 (33), 8502–8511.
  - (17) Jain, S. K.; Tabassum, T.; Li, L.; Ren, L.; Fan, W.; Tsapatsis, M.; Caratzoulas, S.; Han, S.; Scott, S. L. P-Site Structural Diversity and Evolution in a Zeosil Catalyst. *J. Am. Chem. Soc.* **2021**, 143, 1968-1983..
  - (18) Prinsloo, N. M. Preparation of a solid phosphoric acid catalyst from low-quality kieselguhr - Parameters controlling catalyst quality and Performance. *Ind. Eng. Chem. Res.* **2007**, 46 (23), 7838–7843.
  - (19) Ramis, G.; Rossi, P. F.; Busca, G.; Lorenzelli, V.; Ginestra, A. La; Patrono, P. Phosphoric Acid on Oxide Carriers: 2: Surface Acidity and Reactivity toward Olefins. *Langmuir* **1989**, 5 (4), 917–923.
  - (20) Cerruti, M.; Morterra, C.; Ugliengo, P. Surface features of P-doped silica: A comparison between IR spectroscopy and theoretical modelling. *J. Mater. Chem.* **2004**, 14 (22), 3364–3369.
  - (21) Sastre, G.; Lewis, D. W.; Catlow, C. R. A. Structure and stability of silica species in SAPO molecular sieves. *J. Phys. Chem.* **1996**, 100 (16), 6722–6730.
  - (22) Suib, S. L.; Winiecki, A. M.; Kostapapas, A. Surface Chemical States of Aluminophosphate and Silicoaluminophosphate Molecular Sieves. *Langmuir* **1987**, 3 (4), 483–488.
  - (23) Wang, C.; Li, S.; Mao, X.; Caratzoulas, S.; Gorte, R. J. H-D Exchange of Simple Aromatics as a Measure of Brønsted-Acid Site Strengths in Solids. *Catal. Letters* **2018**, 148 (11), 3548–3556.

- (24) Li, S.; Abdelrahman, O. A.; Kumar, G.; Tsapatsis, M.; Vlachos, D. G.; Caratzoulas, S.; Dauenhauer, P. J. Dehydro-Decyclization of Tetrahydrofuran on H - ZSM5: Mechanisms, Pathways, and Transition State Entropy. *ACS Catal.*, **2019**, 9(11), 10279–10293
- (25) Xu, D.; Abdelrahman, O.; Ahn, S. H.; Guefrachi, Y.; Kuznetsov, A.; Ren, L.; Hwang, S.; Khaleel, M.; Al Hassan, S.; Liu, D.; et al. A quantitative study of the structure–activity relationship in hierarchical zeolites using liquid-phase reactions. *AIChE J.* **2019**, 65 (3), 1067–1075.
- (26) Gorte, R. J. What do we know about the acidity of solid acids? *Catal. Letters* **1999**, 62 (1), 1–13.
- (27) Parrillo, D. J.; Adamo, A. T.; Kokotailo, G. T.; Gorte, R. J. Amine adsorption in H-ZSM-5. *Appl. Catal.* **1990**, 67 (1), 107–118.
- (28) Abdelrahman, O.; Vinter, K. P.; Ren, L.; Xu, D.; Gorte, R. J.; Tsapatsis, M.; Dauenhauer, P. J. Simple Quantification of Zeolite Acid Site Density by Reactive Gas Chromatography. *Catal. Sci. Technol.* **2017**, 7, 3831–3841.
- (29) Kofke, T. J. G.; Gorte, R. J.; Farneth, W. E. Stoichiometric adsorption complexes in H-ZSM-5. *J. Catal.* **1988**, 114 (1), 34–45.
- (30) Patet, R. E.; Koehle, M.; Lobo, R. F.; Caratzoulas, S.; Vlachos, D. G. General Acid-Type Catalysis in the Dehydrative Aromatization of Furans to Aromatics in H-[Al]-BEA, H-[Fe]-BEA, H-[Ga]-BEA, and H-[B]-BEA Zeolites. *J. Phys. Chem. C* **2017**, 121 (25), 13666–13679.
- (31) Kofke, T. J. G.; Gorte, R. J.; Kokotailo, G. T. Stoichiometric adsorption complexes in [B]- and [Fe]-ZSM-5 zeolites. *J. Catal.* **1989**, 116 (1), 252–262.
- (32) Chen, H.; Abdelrahman, O. A. Solvating Alkylamine Hofmann Elimination in Zeolites Through Cooperative Adsorption, ChemRxiv Preprint DOI: 10.26434/chemrxiv.14174024.v1..
- (33) Malysheva, L. V.; Paukshtis, E. A.; Kotsarenko, N. S. Deamination of butylamines on the surface of acidic oxide catalysts. *React. Kinet. Catal. Lett.* **1984**, 24 (1–2), 91–95.
- (34) Malysheva L.V.; Paukshtis, E.A.; Kotsarenko, N.S.; Interaction of butylamines with protonic centers of H-NaY zeolite. *React. Kinet. Catal. Letter.* **1984**, 24, 97–101.
- (35) Kester, P. M.; Miller, T.; Gounder, R. Ammonia Titration Methods to Quantify Brønsted Acid Sites in Zeolites Substituted with Aluminum and Boron heteroatoms. *Ind. Eng. Chem.*, **2018**, 57(19), 6673–6683.
- (36) Jones, A. J.; Iglesia, E. Kinetic, Spectroscopic, and Theoretical Assessment of Associative and Dissociative Methanol Dehydration Routes in Zeolites. *Angew. Chemie - Int. Ed.* **2014**, 53 (45), 12177–12181.
- (37) Chiang, H.; Bhan, A. Catalytic consequences of hydroxyl group location on the rate and mechanism of parallel dehydration reactions of ethanol over acidic zeolites. *J. Catal.* **2010**, 271 (2), 251–261.
- (38) Liu, D.; Bhan, A.; Tsapatsis, M.; Al Hashimi, S. Catalytic behavior of Brønsted acid sites in MWW and MFI zeolites with dual meso- and microporosity. *ACS Catal.* **2011**, 1 (1), 7–17.
- (39) Macht, J.; Janik, M. J.; Neurock, M.; Iglesia, E. Mechanistic consequences of composition in acid catalysis by polyoxometalate keggins clusters. *J. Am. Chem. Soc.* **2008**, 130 (31), 10369–10379.
- (40) Zhi, Y.; Shi, H.; Mu, L.; Liu, Y.; Mei, D.; Camaioni, D. M.; Lercher, J. A. Dehydration Pathways of 1-Propanol on HZSM-5 in the Presence and Absence of Water. *J. Am. Chem. Soc.* **2015**, 137 (50), 15781–15794.
- (41) Prestianni, A.; Cortese, R.; Duca, D.

- Propan-2-ol dehydration on H-ZSM-5 and H-Y zeolite: A DFT study. *React. Kinet. Mech. Catal.* **2013**, *108* (2), 565–582.
- (42) Alsalmeh, A. M.; Wiper, P. V.; Khimyak, Y. Z.; Kozhevnikova, E. F.; Kozhevnikov, I. V. Solid acid catalysts based on H3PW12O40 heteropoly acid: Acid and catalytic properties at a gas-solid interface. *J. Catal.* **2010**, *276* (1), 181–189.
- (43) John, M.; Alexopoulos, K.; Reyniers, M. F.; Marin, G. B. Effect of zeolite confinement on the conversion of 1-butanol to butene isomers: Mechanistic insights from DFT based microkinetic modelling. *Catal. Sci. Technol.* **2017**, *7* (14), 2978–2997.
- (44) Alexopoulos, K.; John, M.; Van Der Borght, K.; Galvita, V.; Reyniers, M. F.; Marin, G. B. DFT-based microkinetic modeling of ethanol dehydration in H-ZSM-5. *J. Catal.* **2016**, *339*, 173–185.
- (45) John, M.; Alexopoulos, K.; Reyniers, M.; Marin, G. B. Reaction path analysis for 1-butanol dehydration in H-ZSM-5 zeolite: Ab initio and microkinetic modeling. **2015**, *330*, 28–45.
- (46) Gunst, D.; Alexopoulos, K.; Van Der Borght, K.; John, M.; Galvita, V.; Reyniers, M. F.; Verberckmoes, A. Study of butanol conversion to butenes over H-ZSM-5: Effect of chemical structure on activity, selectivity and reaction pathways. *Appl. Catal. A Gen.* **2017**, *539*, 1–12.
- (47) John, M.; Alexopoulos, K.; Reyniers, M. F.; Marin, G. B. First-Principles Kinetic Study on the Effect of the Zeolite Framework on 1-Butanol Dehydration. *ACS Catal.* **2016**, *6* (7), 4081–4094.
- (48) Konda, S. S. M.; Caratzoulas, S.; Vlachos, D. G. Computational Insights into the Role of Metal and Acid Sites in Bifunctional Metal/Zeolite Catalysts: A Case Study of Acetone Hydrogenation to 2-Propanol and Subsequent Dehydration to Propene. *ACS Catal.* **2016**, *6* (1), 123–133.
- (49) Liu, Y.; Vjunov, A.; Shi, H.; Eckstein, S.; Camaioni, D. M.; Mei, D.; Baráth, E.; Lercher, J. A. Enhancing the catalytic activity of hydronium ions through constrained environments. *Nat. Commun.* **2017**, *8* (March), 2–9.
- (50) Shetty, M.; Wang, H.; Chen, F.; Jaegers, N.; Liu, Y.; Camaioni, D. M.; Gutiérrez, O. Y.; Lercher, J. A. Directing the Rate - Enhancement for Hydronium Ion Catalyzed Dehydration via Organization of Alkanols in Nanoscopic Confinements. *Angew. Chemie* **2021**, *60*, 2304–2311.
- (51) Gao, X.; Heyden, A.; Abdelrahman, O. A.; Bond, J. Q. Microkinetic analysis of acetone hydrogenation over Pt/SiO<sub>2</sub>. *J. Catal.* **2019**, *374*, 183–198.
- (52) Abdelrahman, O. A.; Heyden, A.; Bond, J. Q. Microkinetic analysis of C<sub>3</sub>–C<sub>5</sub> ketone hydrogenation over supported Ru catalysts. *J. Catal.* **2017**, *348*, 59–74.
- (53) Ensing, B.; Laio, A.; Gervasio, F. L.; Parrinello, M.; Klein, M. L. A minimum free energy reaction path for the E2 reaction between fluoro ethane and a fluoride ion. *J. Am. Chem. Soc.* **2004**, *126* (31), 9492–9493.
- (54) Chen, B. W. J.; Mavrikakis, M. How coverage influences thermodynamic and kinetic isotope effects for H<sub>2</sub>/D<sub>2</sub> dissociative adsorption on transition metals. *Catal. Sci. Technol.* **2020**, *10* (3), 671–689.
- (55) Zhi, Y.; Shi, H.; Mu, L.; Liu, Y.; Mei, D.; Camaioni, D. M.; Lercher, J. A. Dehydration Pathways of 1-Propanol on HZSM-5 in the Presence and Absence of Water. *J. Am. Chem. Soc.* **2015**, *137* (50), 15781–15794.
- (56) Kozuch, S.; Martin, J. M. L. “Turning over” definitions in catalytic cycles. *ACS Catal.* **2012**, *2* (12), 2787–2794.
- (57) Gounder, R.; Jones, A. J.; Carr, R. T.; Iglesia, E. Solvation and acid strength effects on catalysis by faujasite zeolites. *J. Catal.* **2012**, *286*, 214–223.
- (58) Knaeble, W.; Carr, R. T.; Iglesia, E.



- Mechanistic interpretation of the effects of acid strength on alkane isomerization turnover rates and selectivity. *J. Catal.* **2014**, *319*, 283–296.
- (59) Macht, J.; Carr, R. T.; Iglesia, E. Elimination Catalysis on Solid Acids. *J. Am. Chem. Soc.* **2009**, *131* (2), 6554–6565.
- (60) Abdelrahman Lab Analytical Tools Webpage (<https://www.umasscatal.com/analytical-tools>) (Date Accessed: 02/22/2021).
- (61) Maduskar, S.; Teixeira, A. R.; Paulsen, A. D.; Krumm, C.; Mountziaris; Fan, W.; Dauenhauer, P. J.; Mountziaris, T. J.; Fan, W.; Dauenhauer, P. J. Quantitative carbon detector (QCD) for calibration-free, high-resolution characterization of complex mixtures. *Lab Chip* **2015**, *15* (2), 440–447.
- (62) H. S. Fogler, Elements of Chemical Reaction Engineering, Pearson Education Inc, Upper Saddle River, NJ, 2006.
- (63) Kresse, G.; Furthmüller, J. Efficient iterative schemes for ab initio total-energy calculations using a plane-wave basis set. *Phys. Rev. B - Condens. Matter Mater. Phys.* **1996**, *54*, 11169–11186.
- (64) Perdew, J. P.; Burke, K.; Ernzerhof, M. Generalized Gradient Approximation Made Simple. *Phys. Rev. Lett.* **1996**, *77*, 3865–3868.
- (65) Blochl, P. E.; Clemens, J. F.; Johannes Schimpl. The Projector Augmented Wave Method : ab-initio molecular dynamics with full wave functions. *Bull. Mater. Sci.* **2003**, *26*, 33–41.
- (66) Kresse, G.; Joubert, D. From ultrasoft pseudopotentials to the projector augmented-wave method. *Phys. Rev. B*, **1999**, *59*, 1758–1775.
- (67) Grimme, S.; Antony, J.; Ehrlich, S.; Krieg, H.; Grimme, S.; Antony, J.; Ehrlich, S.; Krieg, H. A Consistent and Accurate Ab Initio Parametrization of Density Functional Dispersion Correction ( DFT-D ) for the 94 Elements H-Pu. *J. Chem. Phys.* **2010**, *132*, 154104-1–29.
- (68) Grimme, S.; Ehrlich, S.; Goerigk, L. Effect of the Damping Function in Dispersion Corrected Density Functional Theory. *J. Comput. Chem.* **2011**, *32*, 1456–1465.
- (69) Hanwell, M. D.; Curtis, D. E.; Lonie, D. C.; Vandermeersch, T.; Zurek, E.; Hurchison, G. R. Capillary surfaces with free boundary in a wedge. *Adv. Math. (N. Y.)*. **2014**, *262*, 476–483.
- (70) Avogadro: an open-source molecular builder and visualization tool. Version 1.2.0. <http://avogadro.cc/>.
- (71) Brändle, M.; Sauer, J. Acidity differences between inorganic solids induced by their framework structure. A combined quantum mechanics/molecular mechanics ab initio study on zeolites. *J. Am. Chem. Soc.* **1998**, *120*, 1556–1570.
- (72) Tranca, D. C.; Zimmerman, P. M.; Gomes, J.; Lambrecht, D.; Keil, F. J.; Head-Gordon, M.; Bell, A. T. Hexane Cracking on ZSM-5 and Faujasite Zeolites: A QM/MM/QCT Study. *J. Phys. Chem. C* **2015**, *119*, 28836–28853.
- (73) Zimmerman, P. M.; Tranca, D. C.; Gomes, J.; Lambrecht, D. S.; Head-Gordon, M.; Bell, A. T. Ab initio simulations reveal that reaction dynamics strongly affect product selectivity for the cracking of alkanes over H-MFI. *J. Am. Chem. Soc.* **2012**, *134*, 19468–19476.
- (74) Ghorbanpour, A.; Rimer, J. D.; Grabow, L. C. Periodic, vdW-corrected density functional theory investigation of the effect of Al siting in H-ZSM-5 on chemisorption properties and site-specific acidity. *Catal. Commun.* **2014**, *52*, 98–102.
- (75) Nimlos, C. T.; Hoffman, A. J.; Hur, Y. G.; Lee, B. J.; Di Iorio, J. R. Hibbitts, D. D.; Gounder, R.; Experimental and theoretical assessments of aluminum proximity in MFI zeolites and its alteration by organic and inorganic structure-directing agents. *Chem.*



- Mater.* **2020**, 32, 21, 9277-9298.
- (76) Hernandez-Tamargo, C. E.; Roldan, A.; De Leeuw, N. H. DFT Modeling of the Adsorption of Trimethylphosphine Oxide at the Internal and External Surfaces of Zeolite MFI. *J. Phys. Chem. C* **2016**, 120 (34), 19097–19106.
- (77) Kokotailo, G. T.; Lawton, S. L.; Olson, D. H.; Meier, W. M. Structure of synthetic zeolite ZSM-5. *Nature* **1978**, 272 (5652), 437–438.
- (78) Hernandez-Tamargo, C. E.; Roldan, A.; De Leeuw, N. H. A density functional theory study of the structure of pure-silica and aluminium-substituted MFI nanosheets. *J. Solid State Chem.* **2016**, 237, 192–203.